March 2019

Estimating Coastal Water Turbidity Using VIIRS Nighttime Measurement

Chih-Wei Huang
University of South Florida, chihweihuang@mail.usf.edu

Estimating Coastal Water Turbidity Using VIIRS Nighttime Measurement

By

Chih-Wei Huang

A thesis submitted in partial fulfillment
of the requirements for the degree of
Master of Science
College of Marine Science
University of South Florida

Major Professor: Chuanmin Hu, Ph.D.
Brian B. Barnes, Ph.D.
David F. Naar, Ph.D.

Date of Approval:
March 28, 2019

Keywords: VIIRS, remote sensing, DNB, reflectance, sediment front

DEDICATION

This thesis is dedicated to my family: my mother, who has encouraged me in my academic pursuits in the United States; my brother, who has continued to unconditionally support our family while I am away from Taiwan; and my grandmother in Heaven, whose love forever dwells in my heart. I would also like to thank Prof. I-I Lin of National Taiwan University, my pervious advisor and friend in Taiwan, who inspired and emboldened my dreams. Finally, I would like to give thanks to my many friends in Covenant Life Church of Tampa Bay, for the camaraderie and support which they have shared with me over the past three years.

ACKNOWLEDGEMENTS

I would first like to thank my thesis advisor Prof. Chuanmin Hu of the College of Marine Science at the University of South Florida. In his authoritative knowledge and expertise, he has been an invaluable source of guidance throughout this study; without his academic and financial generosity, none of this would have been possible. I would also like to express my gratitude to the rest of my thesis committee: Prof. David Naar, and Dr. Brian Barnes, whose insightful comments and patient encouragement buoyed me through the long editorial process. Especial thanks must go to Prof. David Naar, who supported me tirelessly and charitably in correcting both major and minor errors as they appeared. I am so thankful that you kept me on the right track with your extraordinary knowledge and patience. To all: without your wisdom and patience in the writing process, I would not be able to write this acknowledgment.

A special thanks goes to Dr. Steven Miller of the Cooperative Institute for Research in the Atmosphere at Colorado State University. His knowledge of the lunar model and guidance were invaluable to this study. Many thanks must also go to my colleagues: David English and Jen Cannizzaro for their patient guidance through the relevant field work; Brock Murch for his tireless efforts in keeping the servers running; Shaojie Sun, Mengqiu Wang, and Shuangling Chen for their kindness in sharing class materials and taking the time to teach me image processing. To my friends, especially Jonathan Wong, thank you for your contributions in the editorial process. And to my

neighbor, Rogette Goodhue: thank you for your bottomless patience and selflessness in spending your time as an unpaid English teacher on my behalf to improve my writing and speaking abilities. I cannot overstate my gratitude for your generosity.

Credit is due for the free access to remote sensing data from the National Aeronautics and Space Administration (NASA), the National Oceanic and Atmospheric Administration (NOAA), water turbidity data from the United States Geological Survey (USGS), diagnostic wind data from the National Center for Environmental Predictions (NCEP), and the buoy data from the National Date Buoy Center (NDBC), all of which were crucial for this study. I am also thankful for the software provided by the Optical Oceanography Laboratory of the College of Marine Science, such as ENVI/IDL and SeaDAS. To all those who I could not name here, I must give a collective thank you for your ideas and encouragement in this academic journey.

TABLE OF CONTENTS

LIST OF TABLES

LIST OF FIGURES

ABSTRACT

Coastal water turbidity is a key environmental factor that influences the relative clarity of the water, which therefore reduces sunlight penetration. The comprehensive spatial and temporal coverage of remote sensing allows mapping of water turbidity near the coast. Even in locations where time-consuming and expensive conventional turbidity monitoring programs exist, local technological limitations prevent complete coverage. Traditional optical satellite techniques using the visible band also have limitations in monitoring turbidity due to non-optimal observing conditions such as clouds, sun-glint, and thick aerosols. In this study, in order to complement the daytime satellite measurements, I used the data from Visible Infrared Imaging Radiometer Suite Day-Night-Band (VIIRS DNB), which provides 750 m spatial resolution for a wide band (500 – 900 nm) during nighttime imaging. There were two objectives in this study: (1) Determine the contribution that the nighttime DNB data would provide for estimating turbidity, compared to the VIIRS daytime contribution. (2) Quantify turbidity from the nighttime DNB data in the coastal region. In the Northern Gulf of Mexico, the results showed that the mean monthly nighttime DNB data over the two years can contribute 42.9% of the total usable day and night water pixels. The nighttime DNB data can provide 32.5% of total day and night water pixels that can be used to estimate turbidity, within ±4 days of a full moon. The VIIRS nighttime DNB reflectance data showed a poor relationship with daytime estimated turbidity (R^2=0.61) with a standard error of 7.4 FNU.

The mean relative bias and error were 53.5% and 82.3%. The method used in this study shows promise, but currently still has high uncertainties and errors. Several reasons for these uncertainties and errors were discussed. This study suggests that nighttime DNB data might be useful if uncertainties are reduced through further algorithm development. If so, then during the week of a full moon, nighttime DNB data could be used to calculate nighttime turbidity.

1. Introduction and Background

The main purpose of this study is to determine if coastal water turbidity at night can be quantified using data from a satellite optical observing system, specifically the VIIRS DNB, which stands for Visible Infrared Imaging Radiometer Suite Day-Night-Band. Here turbidity is an optically measured concentration of suspended particles. The suspended particles, including organic and inorganic detritus, can aggregate and be resuspended by wind/wave and tidal currents (Jones et al. 1998). These processes increase the turbidity and the residence time of the suspended particles in water.

Traditionally, water turbidity is measured through the “static” or “dynamic” method (Anderson 2005). The “static method” measures a water sample removed from the source with benchtop meters, while the “dynamic” method uses sensors in the water for instantaneous or continuous monitoring. According to different designs, instruments using the “static method” are preferably used in the lab or on the bigger boats if the conditions allow (e.g., Eutech TB1000 and HACH 2100AN). The instruments designed with the “dynamic” method can be used in the lab with flow-through chambers or in the field with direct measurements (e.g., Rosemount Analytical Clarity II and YSI Environmental 6136). Generally, the measurements taken with these two methods differ. Because the “static” method cannot fully reflect the natural movement of particles, the difference becomes significant when more coarse particles, such as sand, are in the water samples. Through different instruments have different optical designs (Omar and

MatJafri, 2009), the fundamental theory of operation – measuring the amount of scattered light in a sample cell - remains the same (i.e., measure how much light is scattered in a sample cell). There are two turbidity units used by the United States Environmental Protection Agency (US EPA) and European agencies, the Nephelometric Turbidity Unit (NTU) and the Formazin Nephelometric Unit (FNU). The former uses a white light or broadband wavelength with a peak around 400-680 nm. The latter uses monochrome light, which is typically a near-infrared wavelength. Although NTU and FNU are interchangeable (i.e., 1 NTU = 1 FNU), it is recommended that one uses the same instrument design (and unit) for continuous measurements (Anderson 2005).

Mapping turbidity using remote sensing is useful to monitor and assess water quality (Nechad et al. 2010). Due to the comprehensive spatial and temporal coverage, remote sensing can provide important information regarding inland and coastal waters, especially when conventional monitoring programs are hindered by time, cost, and technological limitations (Navalgund et al. 2007). To calculate water turbidity from remote sensing data, a good relationship between *in situ* turbidity and the reflectance of visible red bands is needed. In the Bay of Biscay, Petus et al. (2010) showed a good result in using the 645 nm band from Moderate Resolution Imaging Spectroradiometer (MODIS) in Aqua to model turbidity with a polynomial equation. The R^2 coefficient determined between the calculated turbidity and the *in situ* turbidity was 0.96. In Tampa Bay, Florida, a good relationship was found (R^2=0.73) between remote sensing reflectance at 645 nm [Rrs(645)] versus *in situ* turbidity, when using multiple scattering atmospheric corrections (Chen et al. 2007). The *in situ* data for their project were collected in June 2004, October 2004, and December 2005. The effects of Colored

Dissolved Organic Matter (CDOM) were not significant in Tampa Bay, except for Hillsborough Bay in the wet season (Chen et al. 2007). In southern Finland during 1996-1998, airborne and simulated MEdium Resolution Imaging Spectrometer (MERIS) data (validated by *in situ* data) obtained 79% classification accuracy for five turbidity classes (Koponen et al. 2002). However, optical satellite data still have some limitations. Clouds and sun-glint often block or mask the ocean color data. For example, with nearly full daily coverage, MODIS only provided 19 valid daytime retrievals in a year from a coastal site in the Northern Gulf of Mexico (Chen and Hu 2017). Cloud cover is always an issue for optical satellites since ~68% of ocean is generally blocked by clouds (Eastman et al. 2011; Rossow and Schiffer, 1999). An alternative measurement is needed to obtain more data from the ocean.

VIIRS is one of the five sensors carried on the National Polar-orbiting Partnership (also known as Suomi NPP or S-NPP) Satellite, which is a new generation USA environmental satellite in the (JPSS) Joint Polar Satellite System (Lee et al. 2006; Schueler et al. 2002). VIIRS has 22 channels from the visible band to the long wave IR band. It is also equipped with a panchromatic (DNB) Day/Night Band to provide data under extremely low-levels of radiation at night (Lee et al. 2010). The DNB has a 750-m spatial resolution at nadir and a 3000 km swath width. VIIRS DNB is not the first nighttime radiance provider in the visible spectrum. The (OLS) Operational Linescan System of the U.S. Air Force's Defense Meteorological Satellites was the first night time data provider of the entire planet during 1974-1984 (Croft 1978; Sullivan 1989). However, as a proof-of-concept sensor, the sensitivity of the OLS was rather low. In contrast, VIIRS DNB has better resolution and sensitivity than OLS (Lee et al. 2010),

with a noise floor of 5 x 10^{-7} W m^{-2} sr^{-1}, and a minimum detectable signal of ~3 x 10^{-5} W m^{-2} sr^{-1}.

In general, wavelengths from 400 nm to 750 nm are the most useful in determining constituents in water. The absorption and backscattering of light by constituents influence the water-leaving radiance. Water strongly absorbs light in the long wavelengths (>750 nm), while phytoplankton and CDOM strongly absorb in the blue wavelengths (Matthews 2011). Water turbidity correlates well with reflectance in red bands (Hellweger et al. 2007; Lathrop Jr and Lillesand 1986). Since the DNB covers a wavelength range of 500-900 nm with the central wavelength at 700 nm, VIIRS DNB should be able to quantify coastal water turbidity under sufficient moonlight illumination (Miller et al. 2013). The ability of DNB to detect coastal turbidity dynamics and algal blooms at night has been demonstrated in three case studies of the La Plata River Estuary, Argentine coast, and East China Sea (Shi and Wang 2018). Their study explored the diurnal movement of sediment fronts using DNB radiance ratios in these three different areas.

1.1 Research Objectives

Following the previous studies mentioned above, some unknowns still need attention. For example, there is no study determining the frequency of the available nighttime DNB turbid pixels (i.e., water pixels over a turbidity pattern) over different time spans of days, weeks, months, seasons, or years. Additionally, even though DNB nighttime data allow detection of coastal water turbidity events (Shi and Wang 2018), there is no algorithm developed to retrieve and quantify water turbidity at night. This

study therefore focused on developing an algorithm as explained in the following two objectives.

1) The first objective was to compare the amount of usable water pixels from the night radiance maps with the usable pixels from the daytime data. This comparison assesses whether there is sufficient benefit in working with nighttime DNB data to measure turbidity, with regards to increasing overall temporal resolution, to pursue the second objective. The study regions are located near the Mississippi River Delta and the Atchafalaya Bay (see boxes in **Figure 1**). These regions were chosen, because they are near the most significant river plume in the Northern Gulf of Mexico.

2) The second objective was to use DNB nighttime data to quantify turbidity at night by comparing it to daytime turbidity maps. Previous studies show that visible red bands correlate well with water turbidity (Hellweger et al. 2007; Lathrop Jr and Lillesand 1986). The bandwidth of the DNB data, however, covers a greater wavelength range of 500-900 nm, which includes the red band and the near-IR (infrared) band. The final step of this objective is to develop an algorithm to use the DNB data to quantify nighttime turbidity.

These objectives addressed the following questions:

a) How much do the DNB nighttime data provide in terms of increased observations of turbidity compared to the observations of turbidity from daytime data?

b) Assuming the DNB night radiance pixels have sufficient quality and quantity, how can these pixels be used to estimate coastal water turbidity at night and for how many nights can they be retrieved within a lunar cycle?

2. Research Methods

The different data types are reviewed and a short overview of the data processing is provided in section 2.1. Detailed step-by-step methods for the first and second objectives (sections 2.2 and 2.3) then follow.

2.1 Data Overview

VIIRS nighttime DNB data were used to detect coastal water turbidity events at night. These data were assessed to develop an algorithm to calculate nighttime water turbidity values. VIIRS DNB data can be blocked or obscured by clouds, smoke, and fog. Daytime turbidity maps were calculated from VIIRS remote sensing reflectance at 671 nm and 862 nm (i.e., Rrs(671) and Rrs(862)). To help identify turbidity events, VIIRS true color images were obtained directly from VIIRS Level 1 data. The VIIRS Level 1 and Level 2 data used here are from the NASA Ocean Color Web (https://oceancolor.gsfc.nasa.gov/). Cloud detection at night can be determined by the differences in thermal temperature. The VIIRS IR M15 band, from 10.26 μm to 11.26 μm, was used for the identification of high clouds. The M13 band, from 3.97 μm to 4.13 μm, is important for low cloud and fog detection, due to its smaller wavelength (Ellrod 1995; Eyre et al. 1984; Hunt 1973). VIIRS DNB and IR data are available through NOAA CLASS (https://www.class.noaa.gov/). In order to improve the cloud masking method, VIIRS sea surface temperature (SST) and VIIRS cloud data, such as Cloud

Optical Depth, Cloud Effective Particle Size, Cloud Top Temperature, Cloud Top Height, and Cloud Top Pressure, were entered into custom computer programs to help identify clouds. The two-minute Gridded Global Relief Data (ETOPO2) v2 (National Geophysical Data Center, 2006) were used to mask the land pixels.

The data for this study were downloaded and processed using SeaDAS and ENVI/IDL computer programs developed in-house. I focused on the Northern Gulf of Mexico as a region to map turbidity, because the Mississippi River plume is known to have significant turbidity events. Two years of VIIRS nighttime DNB reflectance maps (from January 2016 through December 2017) were used in this study. The maps with extensive cloud cover were not discarded if there are distinguishable pixels within the maps.

Figure 1 shows the two study regions as red boxes near the mouths of the Mississippi River and Atchafalaya Bay. The coastal waters continuously receive continental waters from the outflow plume of the Mississippi River, making the Northern Gulf of Mexico ideal for studying water turbidity. The distance between Atchafalaya Bay and Mississippi River Delta is about 250 kilometers. The water and sediments in each region come from different local river systems. The sediments from the Atchafalaya Bay are from the Atchafalaya River, a branch of Mississippi River. For the Mississippi River Delta study area, the water and sediments are directly from the distal end of the Mississippi River.

Figure 2 shows a systematic flow chart for data processing and data analyses. In section 2.2 (first objective), the nighttime DNB reflectance maps were characterized using ENVI software, where they were color stretched to enhance the contrast between

the bright targets (i.e., clouds and land) and the adjacent water. This step determined if the reflectance maps were usable for documenting turbidity. The valid pixels were then counted in a computer algorithm to estimate the nighttime DNB contribution. In section 2.3 (second objective), valid nighttime DNB reflectance maps were selected to extract water pixels to match with the derived daytime water turbid pixels. The detailed methods are described below.

2.2 First Objective

A. The Top-Of-Atmosphere (TOA) moonlight irradiance (F_o) for each pixel was calculated using the lunar irradiance model (Miller and Turner 2009), from which the TOA nighttime DNB reflectance was calculated as $R_t = \pi L_t/[F_o \cos(\theta_o)]$, where θ_o is the lunar zenith angle, L_t is the VIIRS DNB nighttime radiance, and F_o is integrated to the bandwidth of VIIRS DNB and weighted according to the VIIRS relative spectral response functions (https://ncc.nesdis.noaa.gov/). The Miller and Turner (2009; online supplement) lunar model was used to obtain F_o. These above steps converted VIIRS nighttime DNB radiance maps to reflectance maps. The boundary used here was 86° - 93°W and 27° - 31°N (**Figure 1**), which contains both study regions shown in the red boxes.

B. The land and cloud pixels were removed from daytime Rrs(671) reflectance maps and from the nighttime DNB reflectance maps to obtain water pixels. Land pixels were identified from ETOPO2 v2 data. Cloud pixels were obtained through my IDL algorithm and VIIRS standard cloud mask data. Note that due to a change in data processing by NOAA, there are two cloud-masking techniques used in this study. The

first is my IDL algorithm that was used for data collected before March 2017. The other is the VIIRS standard cloud mask data from NOAA, which was used for data collected after March 2017.

C. The following steps describe my IDL algorithm: (i) Cloud data were used to identify and remove most cloud pixels. This step removes most of the high clouds, like cirrus and cirrocumulus. To remove other types of high clouds, a combination of different cloud data, such as Cloud Optical Depth and Cloud Effective Particle Size, were used to identify and remove more cloud pixels near the boundary of identified high clouds. (ii) Next, invalid sea surface temperature pixels (as indicated by SST Flags) are treated the same as cloud pixels. (iii) Some middle cloud and low cloud pixels can be identified and removed by comparing the VIIRS IR M15 & M13 radiance maps and nighttime DNB reflectance maps, with each other to obtain a removal threshold. After several comparisons using ENVI software, the removal threshold obtained was 0.20 of DNB reflectance. Note that, for turbid water, the nighttime DNB reflectance ranges from 0.06 to 0.17, which makes 0.20 a reasonable threshold to use. This step also removes most of the thin clouds. However, there were still some cloud pixels difficult to remove using the above steps, especially the cloud pixels along the edge of nimbostratus and cumulus type clouds. (iv) Following several trials, the box-sieving algorithm described below was used to remove those remaining cloud pixels. A moving-box of 25 x 25 pixels over a nighttime DNB reflectance map was used to identify the number of identified cloud pixels from above. If the number is greater than 10, then the remaining pixels that had a reflectance value > 0.05 within that box were considered cloud pixels. Although this algorithm can remove up to 90% of the cloud pixels, it can also accidently remove

some water pixels. A comparison between the VIIRS cloud mask data and my algorithm is shown in the Results Section and discussed in the Discussion Section.

D. Another box-sieving algorithm was used to filter out the pixels that contain unusually high reflectance from the light originating from boats and oil platforms. These pixels show abnormally high nighttime DNB reflectance > 1, which were easily removed from the nighttime DNB reflectance maps. Note that these pixels still include moon-glint pixels. After this step, the remaining water pixels in the nighttime DNB reflectance maps were considered valid VIIRS DNB nighttime water pixels.

E. Daytime water pixels were directly culled from counting pixels from the VIIRS Rrs(671) maps, which represent the remote sensing reflectance values at 671 nm obtained from daytime measurements. Note that the daytime land and cloud pixels were already filtered out in the VIIRS Rrs(671) maps acquired from the NASA ocean color website. Note that these daytime water pixels include sun-glint pixels.

F. To calculate the nighttime DNB contribution in estimating water pixels, including pixels over turbidity patterns, the following equation was applied:

$$DNB\ contribution\ (\%) = 100 \times \frac{VIIRS\ DNB\ nwp}{VIIRS\ Rrs(671)\ pixels + DNB\ nwp} \qquad (1)$$

where *VIIRS Rrs(671)* pixels represent daytime water pixels and *nwp* stands for nighttime water pixels. These daytime and nighttime water pixels include all types of water, but no cloud or land pixels. If there was more than one map of data collected on a certain day, the pixels from each map that overlie each other were added together to count the entire contribution for that day. For example, if there were three VIIRS

nighttime DNB reflectance maps (N1, N2, & N3) and two VIIRS daytime Rrs(671) maps (D1 & D2) in one day, equation (1) would be:

$$DNB\ contribution\ (\%) = \frac{100 \times VIIRS\ DNB\ nwp\ (N1+N2+N3)}{VIIRS\ Rrs671\ pixels\ (D1+D2)+DNB\ nwp\ (N1+N2+N3)} \qquad (2)$$

The *DNB contribution (%)* was calculated for each single 24-hour day (from 0000 GMT to 2359 GMT) using equation (2). The daily *DNB contribution (%)* values were then averaged into a monthly mean. The monthly means were plotted as a time series over two years, with the x-axis representing the month, and the y-axis representing the monthly mean of the DNB contribution over the Northern Gulf of Mexico area defined by 86^{o} - 93^{o}W and 27^{o} - 31^{o}N (shown in **Figure 1**).

G. After calculating the DNB contribution in estimating water pixels, the number of water pixels that could be used to estimate water turbidity were calculated. For both day and night, the water pixels were considered valid only if a turbidity pattern was visible on the corresponding map. All the daytime water pixels were considered valid because turbidity events should always be observable during the day. For nighttime, the valid water pixels are restricted to the best illumination surrounding the time of a full moon.

H. Turbidity events from VIIRS nighttime DNB reflectance maps were labeled as valid cases ("y" cases in **Table 2**) if a turbidity pattern could be clearly observed or distinguished from partial cloud cover. If a turbidity pattern was not completely distinguishable from cloud coverage or there was partial moon-glint, the turbidity events were labeled as potentially valid cases ("y/n" cases in **Table 2**). If there were no

observable turbidity patterns, the nighttime DNB reflectance maps were discarded and not included in **Table 2**.

I. Once a turbidity pattern was identified, all the water pixels from the map were used in the calculation. The equation for the nighttime DNB contribution of turbidity estimates is:

$$DNB\ contribution\ for\ turbidity\ detection\ (\%) = 100 \times \frac{A}{A+B} \qquad (3)$$

where *A* represents VIIRS DNB nighttime water pixels (from the maps with visible turbidity patterns – the "y" cases in **Table 2**) and *B* represents VIIRS daytime Rrs(671) water pixels. The results from this calculation are shown in the Results Section.

J. This study also examines whether wind speed is an important factor for turbidity events in the nighttime DNB data, as it is for daytime turbidity. Wind speed data from buoys in the Northern Gulf of Mexico were acquired from the National Data Buoy Center (https://www.ndbc.noaa.gov/). Four buoys were chosen to represent the Mississippi River Delta and the Atchafalaya Bay. These buoys provide continual data during 2016-2017 and are cover the two study regions. Stations BURL1 (89.428ºW, 28.905ºN) and LOPL1 (90.025ºW, 28.885ºN) are in the Mississippi River Delta. Stations MRSL1 (92.061ºW, 29.441ºN) and EINL1 (91.384ºW, 29.373ºN) are in the Atchafalaya Bay. The wind speed data from buoys are 6-minute or hourly measurements. The wind speed data, measured each hour surrounding the satellite pass time, are averaged at both stations and then with each other. For example, if the satellite pass is at 0717 GMT, then the wind speed from both buoys at 0700 and 0800 GMT were averaged. The

same occurred if the satellite pass time was at 0700 GMT. However, if the pass time were 0659 GMT then wind speed from the two buoys would be averaged from 0600 and 0700 GMT. The comparison between wind speed and nighttime turbidity is shown in the Results Section.

2.3 Second Objective

To estimate daytime water turbidity from remote sensing data, a single band algorithm was used in this study. This objective focuses on the two study regions shown in **Figure 1**, the Mississippi River Delta and Atchafalaya Bay. Following the work of Dogliotti et al. (2015), the turbidity algorithm can be applied to all coastal and estuary waters with a mean relative error of 13.7% and bias of 4.80%. According to Dogliotti et al. (2015), the definition of turbidity follows the International Standard Organization ISO 7027 (ISO 1999). The turbidity unit they used was the Formazin Nephelometric Unit (FNU).

A. The following steps were used to calculate daytime turbidity (T) from remote sensing data of VIIRS Rrs(671) and Rrs(862).

1) The theoretical basis for the single band turbidity algorithm was based on the work from Dogliotti et al. (2014) and Nechad et al. (2009). The Turbidity term, *T*, is described as:

$$T = \frac{A_T^{\lambda}\ \rho_w(\lambda)}{\left(1-\ \rho_w(\lambda)/C_T^{\lambda}\right)} \qquad (4)$$

where $\rho_w(\lambda)$ is defined as the water-leaving reflectance, A_T^{λ} and C_T^{λ} are wavelength-dependent calibration coefficients, and λ is wavelength.

2) The same C_T^λ calibration coefficient from their study was also used in this study. It was calibrated using standard inherent optical properties (Nechad et al. 2009), as follows. C_T^λ is dimensionless, as shown:

$$C_T^\lambda = \gamma \frac{b_{bpT}^*}{a_{pT}^* + b_{bpT}^*} \quad [dimensionless] \tag{5}$$

The absorption and backscattering variables (a & b_b) were calculated from the combination of particulate matter (p) and non-particulate matter (np) as follows:

$$a = a_p + a_{np}, \quad b_b = b_{bp} + b_{bnp} \ [m^{-1}] \tag{6}$$

Dogliotti et al. (2014) and Nechad et al. (2009) assumed that the non-particulate backscatter is negligible with respect to particulate backscatter in turbid waters so that b_{bnp}=0. The turbidity-specific particulate absorption and turbidity-specific backscattering variables were defined as:

$$a_{pT}^* = \frac{a_p}{T}, \ b_{bpT}^* = \frac{b_{bp}}{T} \quad [m^{-1}FNU^{-1}] \tag{7}$$

where $a_{pT}^* = a_p^{*443} e^{(-0.0123(\lambda - 443))}$ and $a_p^{*443} = 0.036 \ m^2/g$ (Babin et al. 2003b). The turbidity-specific backscattering variable was defined as follows: $b_{bpT}^* = 0.02 \ b_p^{*555} b_p^\lambda / b_p^{555}$, where 0.02 is from Mobley (1994) and $b_p^{*555} = 0.51 \, m^2/g$ as described in Babin et al. (2003a) for coastal waters. The ratio, b_p^λ / b_p^{555}, was tabulated

for case 1 and case 2 water (both from 412 to 715 nm) for the Atlantic Ocean, Mediterranean Sea, North Sea, Baltic Sea, and the English Channel in Babin et al. (2003a). Note that the case 1 water is different from case 2 water because its optical properties are dominated by phytoplankton, whereas the case 2 water is any water except for water dominated by phytoplankton (Morel and Prieur, 1977).

3) The calibration coefficient A_T^λ was calibrated using onsite data through non-linear regression analysis (Nechad et al. 2009). The equation is shown as follows:

$$A_T^\lambda = \frac{a_{np}}{\gamma b_{bpT}^*} \quad [FNU] \qquad (8)$$

where A_T^λ is tabulated in Dogliotti et al. (2014) and Nechad et al. (2010).

4) In this study, the water-leaving reflectance, $\rho_w(\lambda)$, is substituted by the VIIRS Rrs(671) multiplied by π. The two calibration coefficients, A_T^λ and C_T^λ, were taken from Dogliotti et al. (2014) and Nechad et al. (2010) and used to calculate turbidity maps from VIIRS Rrs(671) data.

5) The equation for high turbidity values (Dogliotti et al. 2015) was used in this study because the typical turbidity value in coastal inshore waters of the Louisiana Shelf are in the range of 70-120 FNU and the peak value can reach 150 FNU over inland water sites (data from the USGS office in Morgan City, located in the lower Atchafalaya River area - https://waterdata.usgs.gov/usa/nwis/uv?site_no=07381600). Specifically:

$$T = (1-w)T_{671} + wT_{862} \qquad (9)$$

where w is a weighting parameter from 0 to 1 to match when the water-leaving reflectance (671 nm) was between 0.05 and 0.07. T_{671} and T_{862} represent the turbidity calculated from the water-leaving reflectance at 671 and 862 nm, respectively. The mean relative error of this equation was reported to be about 13.7% for the Dogliotti et al. (2015) study.

B. The following steps describe the details of calculating VIIRS nighttime DNB reflectance (R_s).

1) As addressed in the first objective, the TOA nighttime DNB reflectance was calculated as $R_t = \pi L_t / [F_o \cos(\theta_o)]$, where θ_o is the lunar zenith angle and L_t is VIIRS DNB nighttime radiance. F_o is integrated to the bandwidth of VIIRS DNB and weighted to the VIIRS relative spectral response functions (https://ncc.nesdis.noaa.gov/). To remove aerosol contribution and Rayleigh reflectance, the nearest-neighbor approach (Hu et al. 2000) was used in this study. Because only one spectral band is available, it was impossible to carry out the traditional atmospheric correction using two near-infrared bands (NIR) (Gordon and Wang 1994). The nearest neighbor method assumes that the type of aerosol is homogeneous in a relatively small area. The unclear-water pixels were obtained through identified turbidity events in VIIRS nighttime DNB reflectance maps using ENVI software. The clear-water pixels were distinguished from the same maps also using ENVI software. Next, the clear-water pixels close to the turbidity patterns were chosen to calculate a median of R_t. Then, this calculated median of R_t was subtracted from all the R_t values of the unclear-water pixels to create R_s values, which represent the DNB surface reflectance values with respect to clear-water.

Note that this step also assumes that the moon-glint values of the two nearest pixels do not vary significantly.

VIIRS moon-glint data were calculated from satellite zenith and azimuth angles, moon zenith and azimuth angles, and wind speed. The azimuth and zenith angles were obtained from NOAA CLASS. The wind speed data were acquired from National Center for Environmental Predictions (NCEP) Reanalysis 2 (Kanamitsu et al. 2002) provided by the NOAA/OAR/ESRL PSD, Boulder, Colorado, USA (https://www.esrl.noaa.gov/psd/). In the comparison of several turbidity events, the moon-glint values of the chosen clear and unclear-water pixels rarely change more than 0.001 sr^{-1} under typical illumination conditions. These R_S values should generally not be affected by the moon-glint values because most of the moon-glint values should have been removed. However, there were some remaining turbidity pixels with very obvious moon-glint. This was probably due to the moon-glint varying significantly between the remaining pixels (contrary to the assumption above). Those cases were identified and removed using ENVI software and were not used in the nighttime turbidity algorithm.

C. The following steps describe how to establish a nighttime turbidity algorithm using nighttime DNB reflectance.

1) The nighttime turbidity events obtained from the first objective are listed in **Table 2**. Next, the following steps describe how to cull usable events for calculating nighttime turbidity. (i) All “y/n” cases were discarded because their turbidity patterns were hard to distinguish from clouds. (ii) Some “y” cases were discarded if there was sun-glint in the daytime Rrs(671) map or moon-glint in the nighttime DNB reflectance map. (iii) Some “y” cases were discarded because there were no usable daytime

turbidity maps during the same day to compare to a nighttime turbidity event. These steps generate the usable turbidity cases. Each case contained one daytime mapped turbidity and one nighttime mapped DNB reflectance. There were 53 out of 86 turbidity cases culled for developing the turbidity algorithm for nighttime DNB reflectance.

2) To extract usable pixels, both the culled DNB reflectance maps and daytime turbidity maps were processed using ENVI software to select the same region of interest (ROI) over the same turbidity pattern in the study region. Note that some pixels, with a larger satellite view angle (> 60^{o}), were discarded from both daytime and nighttime data maps. Like MODIS, VIIRS has a wide swath ~3000 km. The effects of view angle for VIIRS data could be significant. Image distortion becomes an issue as the view angle away from the nadir view increases (CRCSI, 2017; Xin et al. 2012). This study did not use an algorithm to resolve this issue. Therefore, pixels with a larger satellite view angle are simply discarded.

3) The derived daytime turbidity was used to match with the nighttime VIIRS DNB reflectance. Instead of establishing a pixel-by-pixel relationship, a histogram matching method was used to match these two data sets, according to the cumulative frequency of the data. The method is resilient to slight turbidity pattern shifts between day and night. The number of bins was set to 5000 in order that the bin size could be very small (e.g., 0.0001). After histogram matching, each turbidity event had its own line pattern. Note that the developed algorithm focuses on the major part of the turbidity patterns rather than the extreme values. Therefore, the lowest and highest 1% of the nighttime DNB reflectance data and daytime turbidity estimates were removed.

4) The line patterns from histogram matching were considered a collection of non-linear equations. This study uses the non-linear equations from the Statistical Analysis System (SAS) software to fit the turbidity cases. There were four equations selected by visual inspection (human eye). The best four (out of 19) equations were selected by how well the equations fitted the histogram matching pattern of nighttime DNB reflectance values and daytime turbidity values. These four equations are shown in the Results Section.

5) The following ten equations (10-19) were used to compare the four different equations from step 4 above. The coefficient of determination (R^2) was calculated as:

$$R^2 = 1 - \frac{\sum_{i=1}^{N}\left(Y_{obs}^{i} - Y_{pred}^{i}\right)^2}{\sum_{i=1}^{N}\left(Y_{obs}^{i} - \bar{Y}_{obs}^{i}\right)^2} \qquad (10)$$

where Y_{obs}^{i} is the daytime turbidity, Y_{pred}^{i} is the nighttime turbidity, $\bar{Y}_{obs}^{i}$ is the average of Y_{obs}^{i}, and N is the number of data points. The R^2 gives the goodness of fit for an equation or how well the predicted values match the true data. An R^2=1 means a perfect fit.

The Adjusted R^2 value was calculated as follows:

$$Adjusted\ R^2 = 1 - \frac{(N-1)}{(N-p-1)}(1 - R^2) \qquad (11)$$

where p is the total number of fitted variables in an equation. The adjusted R^2 is usually less than or equal to R^2. This value can be used to compare different equations, when

there are a different numbers of variables in the equations. The R^2 can be misleadingly large when there are more variables in one of the equations being compared to, whereas the adjusted R^2 does not vary as much. This makes the adjusted R^2 a more objective value for comparing different regression equations that have different number of variables.

The Residual variance (unexplained variance), a term that describes the variance that cannot be explained by an equation, was calculated as follows:

$$Residual\ variance = \frac{\sum_{i=1}^{N}\left(Y_{obs}^{i} - Y_{pred}^{i}\right)^2}{N-p} \quad (12)$$

The Standard error of the estimate term was calculated as follows:

$$Standard\ error\ of\ the\ estimate = \sqrt{\frac{\sum_{i=1}^{N}\left(Y_{obs}^{i} - Y_{pred}^{i}\right)^2}{N-p}} \quad (13)$$

This term measures the dispersion between the observations and the regression line. Note that a standard deviation is the dispersion between the observations and the mean of the observations.

The Reduced chi-square (Spiess and Neumeyer, 2010) was calculated as follows:

$$\chi_v^2 = \frac{\chi^2}{N-p} \quad , \text{ and } \chi^2 = \sum_{i=1}^{N}\frac{\left(Y_{obs}^{i} - Y_{pred}^{i}\right)^2}{\sigma_i^2} \quad (14)$$

where χ_v^2 is the reduced chi-square and σ_i^2 is the uncertainty of Y_{obs}^i. In this study, I used 13.7% and 22% from Dogliotti et al. (2015) for equation (14). The χ_v^2 term approaches 1 when a chosen equation fits the observations well. If the term is much larger or smaller than 1, then it means that the true uncertainty of the observations is larger or smaller than the published uncertainties that were used (13.7% and 22%).

The Mean Relative Bias (MRB) and Mean Relative Error (MRE) were calculated as follows:

$$MRB = 100 \times \frac{1}{N} \sum_{i=1}^{N} \frac{\left(Y_{obs}^i - Y_{pred}^i\right)}{Y_{obs}^i} \quad (15)$$

$$MRE = 100 \times \frac{1}{N} \sum_{i=1}^{N} \frac{\left|Y_{obs}^i - Y_{pred}^i\right|}{Y_{obs}^i} \quad (16)$$

where both mean relative bias and mean relative error show the average bias and errors between the observations and predictions.

The 95% of Prediction Interval (PI) term was calculated as follows:

$$upper\ boundary\ of\ PI = Y_{pred}^i + t_{crit} \times SE^i \quad (17)$$

$$lower\ boundary\ of\ PI = Y_{pred}^i - t_{crit} \times SE^i \quad (18)$$

$$SE^i = standard\ error \times \sqrt{1 + \frac{1}{N} + \frac{\left(X_{pred}^i - \bar{X}_{obs}\right)^2}{\sum_{i=1}^{N}\left(X_{pred}^i - \bar{X}_{obs}\right)^2}} \quad (19)$$

where t_{crit} is the t-statistic at 95%, X_{pred}^{i} is the given VIIRS nighttime DNB reflectance in an equation, and the $\bar{X}_{obs}$ is the average of the VIIRS nighttime DNB reflectance from the measurements in the turbidity events. Note that a prediction interval (PI) differs from a confidence interval (CI). The fitted regression line changes when different amounts of data are sampled from a population (i.e., line 1 from sample 1, line 2 from sample 2, etc.). A 95% CI tells that there is a 95% probability that the true best-fit line of that population is within the interval. In contrast, a 95% PI gives a range in which there is a 95% probability that a future measurement from that population will be within that same range (Neter and Wasserman, 1977). Therefore, PI is usually larger than CI and is better to describe the range of true turbidity values at a given DNB reflectance.

6) Two comparisons of daytime turbidity versus nighttime turbidity were made by using one valid example and all of the valid examples shown in **Table 2**. The daytime turbidity was calculated by equation (9) for each valid pixel from the VIIRS Rrs(671) and Rrs(862) maps. To get the corresponding nighttime turbidity, the nighttime turbidity algorithm used the nighttime DNB reflectance value for that same pixel. The result is then shown in a pixel-by-pixel comparison on an XY plot.

3. Results

Preliminary inspection of the nighttime DNB radiance maps under different quarter phases of the moon was encouraging. **Figure 3** shows that, under enough moonlight (84% illumination from the moon for September 9 and 65% for September 11, 2017), turbidity patterns from the Atchafalaya Bay and Mississippi River plumes are observable. The two panels in **Figure 3** represent results 3 and 5 days after the full moon. Note that the day of the full moon (100% moon illumination) was on September 6. Red arrows in **Figure 3** show the river plumes, comprised primarily of suspended particulate matter. The nighttime DNB radiance unit is μW cm^{-2} sr^{-1}. The lunar irradiances for the two time periods are 0.048 and 0.022 μW cm^{-2} respectively, as calculated from a lunar model. **Figure 3** also shows examples that could be usable turbidity events. The following sections describe the results of the first objective and second objective.

3.1 First Objective

This objective is to estimate the VIIRS DNB nighttime contribution of turbidity estimates. The first step is to count valid water pixels in the night and day data maps, as described in the Research Methods section. By comparing the valid nighttime and daytime water pixels, it can be shown that the monthly VIIRS DNB nighttime data contribution ranges from a minimum of 30.6% to a maximum of 62.5% of the total

daytime and nighttime water pixels available from 2016 to 2017 (**Table 1**). The monthly mean in 2016 and 2017 are 36.3% and 49.6%, respectively. Overall, nighttime DNB data contributes 42.9% of total water pixel detection, which is a significant increase of potential observations of possible water turbidity.

Figure 4 shows the data in **Table 1** as a time series. By plotting the data, it is clear that nighttime DNB contribution is different before and after March 2017. The ~13% difference (i.e., 36.3% in 2016 and 49.6% in 2017) is due to the different approaches used to remove cloud pixels, as previously stated in the Research Methods Section. The lower DNB contribution suggests that the nighttime DNB water pixel contribution could be underestimated before March 2017. The calculation of my algorithm may have been overly aggressive, as shown in **Figure 5**. The average difference of DNB water pixel contribution in 2017, when using the two methods in cloud masking, is 17.8% (**Figure 5**). This result is discussed further in the Discussion Section.

After determining the DNB water pixel contribution, the next step was to estimate nighttime DNB's ability in detecting turbidity events, as compared to daytime Rrs(671) data. First, the identified turbidity events are shown in **Table 2**. The data shown in **Table 2** consist of 86 events indicated as "y" and 47 events are "y/n". The "y" means that the turbidity pattern was identifiable and the water pixels over the turbidity pattern were able to be separated from the nearby cloud pixels. However, if the water pixels were difficult to distinguish from clouds over a turbidity pattern, the events were labeled as "y/n". The "y/n" cases also include moon-glint events.

All the data in **Table 2** have been organized and quantified according to the day and corresponding moon phases in **Figure 6**. Over the two-year period (2016-2017),

there were 133 nighttime turbidity events (“y” & “y/n” cases) ranging from full moon -10 days to full moon + 6 days. To narrow down the range, there were 119 out of 133 events in the range of full moon ±4 days. Note that there were total of 381 valid and invalid events (i.e., including those reflectance maps that do not show turbidity patterns) in the range of full moon ±4 days during 2016-2017. DNB data contribution can be classified as “y” and “y/n” using the one criterion that a turbidity event can be seen on a nighttime DNB reflectance maps. The results of this classification suggest that turbidity patterns during the week of a full moon could be observed in about 31% of all the nighttime DNB mapped reflectance data. In my study area, there were total of 42 reflectance maps when a full moon occurs. Note that sometimes, there can be up to 3 nighttime DNB reflectance maps obtained during any given night in the Northern Gulf of Mexico, due to the S-NPP satellite’s orbital period of 1.7 hours. Only 22 out of the 42 maps showed turbidity patterns, i.e., about 52% of total reflectance maps, including “y” and “y/n” cases, turbidity patterns could be seen during this period of sufficient moonlight illumination.

To inspect whether wind speed is also an important factor for nighttime DNB’s turbidity events, wind speed data from National Data Buoy Center are used. There are two primary questions. Does wind speed correlate with nighttime turbidity events? **Figure 7** shows the wind speed measurements during 2016-2017, with the corresponding “y” and “y/n” turbidity cases from **Table 2**. Wind is usually a cause of strong waves and re-suspension of sediment from shallow depths leading to high water turbidity. During the turbidity cases in the Mississippi River Delta, the wind speed ranged from 3.2 to 10.6 m s^{-1}. There were 19 out of 83 cases with the speed less than 5

m s^{-1}. For cases in the Atchafalaya Bay, it is from 2.6 to 7.1 m s^{-1}. There were 49 out of 101 cases with the speed less than 5 m s^{-1}. In **Figure 7**, the “y” and “y/n” turbidity cases are scattered in a wide range of wind speed. The weakest wind speed observed with a turbidity case was 2.6 m s^{-1} while the strongest wind was 10.6 m s^{-1}. Through VIIRS nighttime DNB data, turbidity cases were revealed during both weak wind and strong wind conditions. Those turbidity cases were mostly visible in the range of full moon ± 4 days. This result shows that the wind speed does not appear to correlate with turbidity during time of visible VIIRS nighttime DNB turbidity cases.

The second question is focused on the pattern of turbidity. Is the wind speed an important factor in the size of turbidity patterns? **Figure 8** shows consecutive nighttime DNB reflectance maps in the Atchafalaya Bay and the Mississippi River Delta. In (a) through (d), the figure panels are 3 to 6 days past the full moon. The turbidity patterns, shown in (a) through (c), change significantly (as can be seen in the color changes representing reflectance values), whereas (c) and (d) are similar. The wind speed in panels (a)-(d) are 4.9, 4.8, 5.1, and 5.3 m s^{-1}, which vary less than 0.5 m s^{-1} variation over the same period. Thus, the changes in the turbidity pattern (a)-(d) occur during relatively constant wind speeds, which do not vary more than ~10%. In fact, the small increase in wind speed shows a decrease in the size of turbidity pattern (**Figure 8**). In (e) through (g), three maps are shown from the Mississippi River Delta although the image on June 22 is excluded because of clouds cover. The maps are 1~4 days past the full moon and the wind speeds are 4.2, 3.7, and 3.8 m s^{-1}. In comparison to the size of the turbidity pattern just outside the delta, the turbidity pattern in (e) and (g) is more scattered than in (f). The wind speed in (e), (f), and (g) remains relatively constant (i.e.,

varies less than 14%). However, the analysis is very rough here. The limitations of these results are addressed in the Discussion Section.

The steps to estimate the nighttime DNB's contribution of usable water pixels for turbidity estimation follows. Only "y" cases in **Table 2** were selected. First, to obtain the DNB's contribution, the nighttime water pixels in the "y" cases were divided by daytime water pixels during the whole month. The results are shown in **Table 3**. The DNB monthly contribution to estimate water turbidity ranges from 2.7% to 39.9%. The monthly variation in **Table 3** is due to different amounts of cloud cover in each month. Although most of the contribution is from daytime data, the mean of nighttime DNB monthly contribution in 2016 and 2017 is 14.3% and 16.9%, which is significant. Over the two years, the mean nighttime DNB data contribution is 15.6%.

Second, it is clear that most of the "y" cases were near the full moon phase within the range of ± 4 days, as shown in **Figure 6**. **Table 4** shows the calculated contribution only during this 9-day period (for both daytime and nighttime data). After the data were selected in the range of the full moon ± 4 days, nighttime DNB monthly contributions can range from 6.32% to 57.8%. Compared to the result in **Table 3**, the mean contribution in 2016 and 2017 is doubled to approximately 30.3% and 34.7%, respectively. The monthly variation in **Table 4** is due to different amounts of cloud cover during the full moon phase each month. For 2016 and 2017, the 30.3% and 34.7% contribution from nighttime DNB contribution suggest that the DNB could be useful in estimating turbidity close to and during the full moon phase. Over the two years, the mean nighttime DNB contribution is 32.5%.

Figure 9 shows the results of same calculation, but focuses on the Atchafalaya Bay and the Mississippi River Delta study areas during ± 4 days of each moon. The DNB contribution can be over 50% from March to May as shown in **Figure 9**. For the rest of year, it is below 50%, probably due to increased cloud cover. For the Mississippi River Delta, the mean contribution is 32.8%, and 36.0% for the Atchafalaya Bay. The highest value reached is 83.4%, and the lowest is ~6%. The large range of percentages is due to the variations of cloud cover. When zooming in on smaller regions (i.e., these two smaller study areas), clouds become more important. The nighttime DNB mapped reflectance can be completely cloud free and then become blocked by clouds that arrive quickly the following day. Overall, the mean of the two study regions combined is 34.4% during 2016-2017.

3.2 Second Objective

This objective was to derive an algorithm to estimate water turbidity at night. Daytime derived satellite turbidity estimates were then compared to the VIIRS nighttime DNB reflectance. The result of this objective can be used as an approach to estimate water turbidity in estuaries. To accomplish this, daytime VIIRS data, including Rrs(671) and Rrs(865), were processed to derive daytime turbidity using the Dogliotti et al. (2015) method of estimating water turbidity, which has been validated in many areas around the world, such as Southern North Sea, French Guyana, Scheldt, Gironde, and Río de la Plata estuaries. Although the algorithm from Dogliotti et al. (2015) has not been tested in the Northern Gulf of Mexico, I used their mean relative error and mean bias from their other studies, which is about 13.7% and 4.8%, respectively. **Figure 10** shows

an example of a comparison with a VIIRS true color image, VIIRS Rrs(671), and a derived VIIRS daytime turbidity map in the Northern Gulf of Mexico. As shown in **Figure 10**, the turbidity pattern in the derived daytime turbidity map is very close to Rrs(671) and the true color image. Therefore, the derived daytime turbidity can then be used to match with the VIIRS nighttime DNB reflectance data to approach nighttime water turbidity.

There are 86 identified nighttime turbidity events (i.e., labeled as “y” in **Table 2**) that were the combination of cases in Atchafalaya Bay and the Mississippi River Delta. Note that some cases showed turbidity events in the both regions in the same day. **Figure 11** shows a distribution pattern based on the value and frequency of the daytime turbidity from 86 turbidity maps derived from VIIRS Rrs(671) and Rrs(862). The majority of the calculated turbidity values range from 0 to ~20 FNU. These turbidity values are located near and away from the coastal regions. Close to the inland regions, the turbidity value can reach up to ~60 FNU. However, this value is less than the *in situ* measurements that can reach up to ~120 FNU [e.g., data from the USGS office in Morgan City (https://waterdata.usgs.gov/usa/nwis/uv?site_no=07381600), located in the lower Atchafalaya River area]. This influence is addressed in the Discussion.

Before using histogram matching method, a pixel-by-pixel matching was used to see the correlation. **Figure 12** shows a scatter plot of six cases from the Atchafalaya Bay and the Mississippi River Delta. **Figure 12** does not show a good fit of the paired data, which makes it difficult to develop a linear equation. This is mainly caused by the variation in the turbidity pattern over a ~ 12-hour period from day to night. Therefore, an

alternative strategy, a cumulative histogram matching method, was used in order to look for a better correlation.

Next, **Figure 13** shows the cases of the histogram matching method, which was then used to draw a new scatter plot. The selected pixels are shown in the right panels as the XY plot of the nighttime DNB reflectance and turbidity, based on the cumulative frequency of the left panels. The result in **Figure 13** is much better than in **Figure 12** because the line patterns do not spread out and seem to be more stable. Therefore, by using histogram matching method, a more stable relationship can be derived than by using the pixel-by-pixel matching method.

As addressed in the Research Methods Section, 53 usable cases were culled from 86 cases in **Table 2**. The nighttime DNB reflectance and daytime turbidity data are visible in both study regions. Note that these cases have not been completely separated according to their location in **Figure 14**a. For example, there are some cases that the turbidity patterns can be seen in both the Atchafalaya Bay and Mississippi River Delta in **Figure 14**a. However, in **Figure 14**b they were separated by their location. **Figure 14**a shows all 86 cases before sieving. **Figure 14**b indicates the 53 cases, which are culled and separated into two study regions. These 53 cases include 34 cases in the Atchafalaya Bay and 19 cases in the Mississippi River Delta. They were drawn together in **Figure 14**b and were the result of removing the lowest and highest 1% of the data from the nighttime DNB reflectance and daytime turbidity estimates as previously mentioned in the methods section. As shown in **Figure 14**, the difference between sieving is obvious (a vs. b), and thus b is a better selection to develop the nighttime turbidity algorithm.

Figure 15 is similar to **Figure 14**b. The purpose of **Figure 15** is to see if there is a big difference between the two study regions. **Figure 15** shows that the matched results from histogram matching are nonlinear. The daytime turbidity appears to increase exponentially with increasing nighttime DNB reflectance. Each case in the two study regions shows a different type of exponential shape. When comparing the patterns between the Mississippi River Delta and the Atchafalaya Bay, the overall patterns are similar. Both the data patterns in the two study regions are less scattered when nighttime DNB reflectance is below 0.04 and daytime turbidity is less than 15 FNU. When nighttime DNB reflectance is above 0.04, the data patterns in **Figure 15** become more scattered. Although it is possible to develop two different algorithms for the two study regions, the purpose of this study is to develop one algorithm to estimate nighttime water turbidity in both study regions. Therefore, I combined the 53 cases in the Mississippi River Delta and the Atchafalaya Bay to develop one algorithm.

Four equations were chosen from a group of non-linear equations in SAS software to fit the data relationship **Figure 14**b, as detailed in the Research Methods Section. **Figure 16** shows the density plot of the 53-paired data, the fitted regression curves resulting from the four equations, and some of the statistics from **Table 5** and **Table 6**, such as the error bars and the 95% prediction intervals.

Equation number 1 was chosen as the equation that best fits the data (**Figure 16**). In **Table 5**, the standard error of the estimate is around 7.4 FNU for the four equations. In **Table 6**, the standard error significantly increases as the given nighttime DNB reflectance increases. This was determined by calculating all dispersion points at a given nighttime DNB reflectance. The standard deviation of the turbidity and the

standard error of the estimate show that, after 0.04 of nighttime DNB reflectance, the predicted turbidity has a greater uncertainty. Neither the standard deviation nor standard error can give a range of the prediction. The 95% prediction interval in **Figure 16** and **Table 6** shows that, at a given nighttime DNB reflectance, there is 95% probability that the true nighttime turbidity will lie within the interval (i.e., predicted turbidity ± 14.5 FNU).

The adjusted R^2 in **Table 5** shows that these four equations could only interpret 60-61% of turbidity changes. In comparison of the four equations, they show a close number of the standard error of estimate and the adjusted R^2, while only equation 1 has a better result regarding relative mean bias and uncertainty. The reduced chi-square is also a measurement that helps decide which equation is better (Rhinehart 2016; Spiess and Neumeyer 2010). In an effort to assign an uncertainty to the reduced chi-square calculation (Spiess and Neumeyer 2010), recall that two published uncertainty values of 13.7% and 22.0% were used. The former uncertainty is the published mean value from Dogliotti et al. (2015). The latter uncertainty is from the Southern North Sea, which is an area with a similar turbidity range as the Northern Gulf of Mexico (Dogliotti et al. 2015). Typically, the reduced chi-square would be close to 1 when the equation fits the data well. When the reduced chi-square is over 10, it shows that no equations fit the data well, as mentioned in the Research Methods Section. **Table 5** shows the chi-square values when using both uncertainties. **Table 5** clearly shows that none of these equations, with either uncertainty, fit daytime derived turbidity data. Because the data are too scattered to fit by these different equations, they are not useful to accurately interpret the data. However, equation 1 shows the best lower mean relative bias and

error (i.e., 53.5% and 82.3%) out of the four equations considered. Therefore, the equation 1 is better than other equations and was chosen to calculate a rough estimate of the nighttime turbidity.

Figure 17 shows a comparison between histogram matching and pixel-to-pixel matching methods, which both use the same type of equation as equation 1. **Figure 17** shows that the pixel-to-pixel matching relationship is poor probably because the matched pixels are too incompatible to match. The adjusted R^2 for the histogram matching method is 0.61, while it is only 0.26 for the pixel-to-pixel matching method. This comparison indicates that the histogram matching method is preferred over the pixel-to-pixel matching method. **Table 7** is a summary comparison between daytime turbidity and nighttime turbidity in equation 1 in **Figure 16**. In **Table 7**, there were 27 cases with mean relative error less than 50.0%, while there were 26 cases that signified more than 50.0%. When comparing cases in the Atchafalaya Bay with cases from the Mississippi River Delta, the cases from the Atchafalaya Bay had a relatively lower error than the cases from the Mississippi River Delta. As shown in **Table 7**, the highest mean relative error is 433% in the Mississippi River Delta and lowest value is 13.9% in the Atchafalaya Bay.

Figure 18 shows one example of a selected case showing different mean relative uncertainties on the Louisiana Shelf (i.e., 17.3% in the Atchafalaya Bay & 71.4% in the Mississippi River Delta). In **Figure 18**, the daytime turbidity and estimated nighttime turbidity are different because equation 1 can only fit 61.0% of turbidity changes (**Figure 16**). There are some uncertainties in both calculated daytime turbidity and nighttime DNB reflectance. Although the estimated nighttime turbidity estimates do

not match with daytime turbidity values well, the nighttime DNB estimated turbidity could still be used as a very rough approximate estimate of nighttime turbidity when daytime data are not available. More detailed are discussed in the next section.

4. Discussion

4.1 DNB Contribution

VIIRS nighttime DNB imagery has been found to have the potential to complement daytime data. The method of cloud masking used in this study was performed in two ways: my own algorithm, and the VIIRS standard cloud mask product method, which became available later within the time frame being studied. As detailed in the Research Methods Section, the algorithm I used combines the bad pixels indicated in VIIRS SST Flag product with the valid pixels in VIIRS cloud products. However, this method can only remove pixels with strong contrast of infrared radiance. The final step of the box sieving was also performed to filter the remaining cloud pixels. However, the DNB values of pixels over low clouds and turbidity patterns are very similar in many cases, where my algorithm might filter valid water pixels and thus be too aggressive in attempting to filter out pixels with low cloud cover. VIIRS cloud mask data, which became available in March 2017, shows a difference compared to my algorithm (**Figure 5**). My cloud mask algorithm caused an average underestimate, 17.8%, from March 2017 to December 2017. Additionally, a second sieving was done to mask the lights from fishing boats and oil platforms at night. The sieving was based on nighttime DNB reflectance to remove one or two pixels with extremely high reflectance over the background value. This sieving was not applied to the daytime pixels, which is a possible reason that nighttime DNB data shows a lower contribution.

A major limitation for VIIRS nighttime DNB detection of turbidity patterns is the amount of available moon light (or intensity). It is clear that from **Table 2** most turbidity events are ±4 days of the full moon. Generally, turbidity events are visible in almost every daytime map when it is not blocked by clouds while the nighttime DNB data only reveal turbidity events when there is sufficient moon light and cloud-free skies. Note that even during the full moon ±4 days with a cloud-free sky, the nighttime DNB data occasionally could not reveal turbidity patterns. In using nighttime DNB data, it is clear that the turbidity cases need to be determined on a case-by-case basis. It is possible that part of missing data from the remapping of nighttime DNB images (Hillger et al. 2014) could play a role for DNB's relatively low contribution.

Another limitation of detecting turbidity patterns at night is the variation of clouds from the day to night. The monthly climatology observations between the boundaries of land and ocean, shows that generally there are more clouds/precipitation occurs at night than during the day along the Louisiana and Mississippi offshore regions (Hill et al. 2010). In general, the heat capacity of land and ocean is different, which leads to the variance of surface temperatures through a 24-hour cycle in which the temperatures over land change faster than over water. Specifically, the surface temperature on land is usually higher than the ocean during the day, leading to more chance of clouds developing over land during the day and vice versa (i.e., the land temperature becomes cooler than the water temperature, leading to cloud formation over the water at night). This diurnal difference of the temperature causing the reverse of wind direction along the coastal areas is a well-known climatology phenomenon, known as sea and land breezes. However, it would be too simplistic to state that sea and land breeze is the

main reason leading to more clouds in my study regions. A developed regional numerical weather model is needed to investigate the contribution of other factors, such as tropical storms, cold fronts, and mesoscale convective systems.

The preliminary inspection of the influence from wind speed is a qualitative attempt to search for correlation between wind speed and nighttime DNB data derived turbidity. Theoretically, high wind can influence water turbidity by introducing larger waves and re-suspension of sediment from shallow depths. However, it is hard to determine if these wind conditions influenced turbidity patterns, as shown in **Figure 8** and **Figure 9**. The identified nighttime turbidity events tend to become clearer when closer to time of the full moon. The size of turbidity patterns at night appears to depend on amount (intensity) of moon light. For nighttime DNB data, moonlight intensity is the most important factor to detect nighttime turbidity. This preliminary investigation of nighttime wind speed patterns versus nighttime turbidity patterns did not show any correlation. The nighttime turbidity changed while the winds remained similar. More information, such as wind direction, the duration of wind, *in situ* measurements of turbidity, and an air-sea interaction model will be need to conduct a more detailed investigation on the effect of wind speed over nighttime water turbidity.

4.2 DNB Estimated Turbidity

A single band turbidity algorithm used in this study was to assess DNB's ability to estimate water turbidity at night. To retrieve water turbidity, Dogliotti et al. (2015) suggested the use of 645 nm (MODIS band) for low to medium turbidity and 859 nm (MODIS band) for medium to high turbidity. In this study, the two wavelength-dependent

calibration coefficients, A_T and C_T, are adopted from MODIS bands in Dogliotti et al. (2015). The results from this step in my study suggests a possible nighttime bias in estimating turbidity, even though the two wavelengths used in VIIRS and MODIS sensor systems are relatively close to each other.

The use of water reflectance on 862 nm in my study to estimated medium to high turbidity might be questionable because Dogliotti et al. (2015) has not clearly demonstrated which atmospheric correction was used in their study. In this study, the Level 2 VIIRS Rrs(671) and Rrs(862) data were downloaded from NASA Ocean Color website (https://oceancolor.gsfc.nasa.gov/), which uses the Near-Infrared (NIR) bands for atmospheric correction. The method assumes that NIR water-leaving radiance is negligible, which is suitable for clean open water. However, Short-Wave-Infrared (SWIR) bands for atmospheric correction is usually recommended (Pahlevan et al. 2017; Vanhellemont and Ruddick 2015) for very turbid waters, because the negligible NIR assumption can be invalid and cause an overcorrection when removing the atmospheric effects (Siegel et al. 2000). The use of the NIR assumption for atmospheric corrections in daytime turbidity may lead to additional uncertainties for the derived daytime turbidity, as discussed next.

In **Figure 11**, the derived daytime turbidity from VIIRS Rrs(671) and Rrs(862) reaches up to a maximum ~60 FNU while the *in situ* measurements from the USGS office in Morgan City can reach ~120 FNU. This leads to some unknowns in the derived daytime turbidity. Additionally, in the VIIRS Rrs(671) and Rrs(862) reflectance maps, some coastal areas were masked as the missing data, as shown in **Figure 10**. These missing data are described as “Moderate sun glint contamination” and “Failure in any

product” in the online document (https://oceancolor.gsfc.nasa.gov/atbd/ocl2flags/) from NASA Ocean Color website. The reason for the missing data is likely due to their use of the NIR atmospheric correction method (and assumption). However, these missing data were identified as turbid pixels in the true color images and were likely to have high turbidity values. For example, when the observations are closer to coastal regions, higher turbidity is usually observed. These missing daytime data suggest that the derived turbidity algorithm for nighttime DNB reflectance will be more useful in a lower turbidity range because of the algorithm’s dependence in matching to the daytime turbidity. How to retrieve these higher missing daytime turbidity values will need further inspection, and if resolved, may lead to an improved nighttime estimate of turbidity.

There are also some uncertainties in VIIRS nighttime DNB water reflectance data. There is no atmospheric correction for VIIRS nighttime DNB data. To get water reflectance in this study, a nearest-neighbor approach (Hu et al. 2000) was used to remove influence from aerosols and Rayleigh scattering. However, the accuracy of this approach is unknown when applied to the nighttime DNB data. It is important to find valid non-turbid pixels in the DNB data images for comparisons. In the Louisiana Shelf, water is rarely clear because of the large degree of suspended sediment directly or indirectly arriving from the Mississippi River. Any non-clear water pixel can lead to higher surface reflectance and cannot represent a valid clear water pixel. The path radiance is also different if the selected non-turbid pixels are far from the region of interest. It is obvious that this approach can result in some uncertainties calculating nighttime DNB water reflectance in this study. Perhaps a future study using large holding tanks or retention ponds that can allow the sediment to settle or be filtered out

and, in turn, may help reduce this uncertainty of what represents a true clear water pixel in this area.

Another uncertainty is the lack of true nighttime water turbidity data measured *in situ*. The daytime derived turbidity from VIIRS Rrs(671) and Rrs(862) was used to approximate the true daytime water turbidity. The nighttime DNB water reflectance over turbidity patterns is supposed to allow an estimation of the nighttime water turbidity. The histogram matching method helped develop a good fit between nighttime DNB reflectance data and daytime turbidity data when the turbidity pattern slightly shifts between day and night. However, the uncertainty of this approach is not well known. The time gap between day and night observations is about 12 hours. During such time gaps, significant changes to the water properties and cloud cover can occur, especially when considering the general surface water speed is around 0.54 m s^{-1} in the two study areas (https://www.nps.gov/miss/riverfacts.htm). Tides and strong winds are the primary factors, which drive coastal water motion. The lateral resolution of the DNB data is about 1 kilometer. The irregular flow of the river plumes outside Atchafalaya Bay and the Mississippi River Delta is expected to result in uncertainties. Additional attention in determining these uncertainties would be helpful.

Figure 19 is an example of how sediment moves in the four consecutive maps. The sediment front is labeled in (b), (c), and (d), as a red, green, and blue line. Considering the minimum linear distance along the black solid line (i.e., labeled in (d)) to the closest point at shore, the offshore distances are: 13.6 km for the red line in (b), 24.4 km for the green line in (c), and 16.1 km for the blue line in (d). Compared with the time interval, the mean speed of the sediment front along the black solid line was ~0.24

m s^{-1}. The speed can also be calculated along the white solid line in (d), as ~0.23 m s^{-1}. **Figure 19** shows a good example of DNB's ability to detect the relocation of a sediment front. When daytime data are not available, the nighttime DNB data can be used to estimate or predict sediment fronts in coastal models. However, it is noticeable that nighttime DNB reflectance can give a broad estimate, but not as accurate as the daytime data, which are shown in (a) and (c) of **Figure 19**.

Prior to this study, Shi and Wang (2018) developed an approach by using a ratio (DNB radiations ratio) between the target radiance and the reference radiance to assess ocean diurnal environmental changes with VIIRS DNB data. Note that their method was able to filter background noise and improve the signal to noise ratio of the original DNB observations. For the method used in this study, the lunar illumination of is the key to observe and estimate nighttime turbidity. **Figure 20** illustrates the difference between the two methods. The DNB radiations ratio method used in their study seems to be more straightforward in enhancing DNB observations over ocean waters, but it is limited to cloud free sky or maps with sporadic isolated cloud conditions, as shown in (a) of **Figure 20**. The advantage of the nighttime DNB reflectance used in this study is that cloud pixels, fishing boats, and oil platforms can be mostly removed and yet leave useful pixels for analysis. The resulting reflectance maps can be used to estimate nighttime water turbidity, as shown in (b), (c), and (d) of **Figure 20**. The original map (b) has the pixels associated with clouds and lights from oil platforms and boats removed from it and shown as (c) which leaves the final processed map (d). Note that there is some clustering of removed pixels surrounding the cloud edges shown in **Figure 20**c,

which may not be lights from boats or oil platforms, but rather remaining cloud pixels that were not properly masked.

Both methods of estimating nighttime turbidity are influenced by moon-glint and lack of lunar illumination. Since both methods can be used to observe turbidity patterns, they could be used to assess and compare their relative error and bias if the nighttime *in situ* turbidity data are available in the future. One item of note in these two methods is that the diffuse glow from city lights in coastal regions was found to add to the nighttime DNB data. This additional light source will likely be a problem by increasing uncertainty when estimating nighttime turbidity because it is hard to separate the contribution of artificial light from moon light. Perhaps city lights may provide sufficient light for alternative uses of the DNB nighttime data, such as monitoring shallow urban coastal waters. Clearly more research is needed to improve the use and accuracy of nighttime DNB water reflectance data for nighttime measurements, especially near suburban areas.

One example of the comparison of nighttime and daytime turbidity is shown in **Figure 21**. The R^2 is 0.69, while the slope is 0.4. Assuming that water turbidity did not change between day and night, the data show that the nighttime turbidity is underestimated above 30 FNU daytime turbidity. A comparison of all 53 usable cases from **Table 7** is illustrated in **Figure 22**. The overall average trend shows lower nighttime turbidity when daytime turbidity is greater than 10 FNU. The reason is unclear, but probably due to a systematic error in the algorithm. Other potential sources of error might be related to some of the assumptions discussed earlier, the wide bandwidth of the DNB data versus the two single bands used in the VIIRS data, or perhaps to the

moon phase as it waxes to and wanes from a full moon. The DNB data have a wide wavelength range and the DNB data spectral response function is not 100% in all its spectral wavelengths (Miller et al. 2013). The relative response gradually increases from 500 nm, peaks at 700 nm, and then drops to 900 nm. Both the relative spectral response from the 671 nm and 865 nm wavelengths are about 0.85-0.9, whereas it is about 1.0 from the 700 nm wavelengths (Miller et al. 2013). Therefore, it is speculated that the uneven spectral response might lead to this underestimate. Future work would be necessary to investigate all the potential sources for these errors.

5. Conclusions

In this study, VIIRS nighttime DNB data were assessed in two ways. The first is to estimate how much they can contribute to water pixel measurements over a 2-year period from January 2016 to December 2017. In general, the monthly DNB data contribute 42.9% of total water pixel detection. The second is to investigate their contribution in estimating water turbidity patterns over two years. The VIIRS nighttime DNB data contribute 32.5% during ±4 days of the full moon. The average number for the Atchafalaya Bay and the Mississippi River Delta is 34.4%. The main uncertainty is from the variation of clouds. Two cloud masking methods were compared in this study. The result shows that the DNB contribution underestimate 17.8% during March 2017 to December 2017, most likely due to two different cloud masking algorithms being used. The analysis in this study suggests that, under appropriate illumination, DNB nighttime data can be a useful complement especially when daytime turbidity estimates are not possible due to daytime cloud coverage. The algorithm developed in this study shows that only about 61% variation of turbidity can be interpreted. The standard error of the estimate is ~7.4 FNU. The 95% prediction interval shows that any true turbidity value at a given nighttime DNB reflectance will lie with the predicted turbidity ±14.5 FNU. The main limitation of the method and equation used is that it is currently restricted to coastal regions where turbidity variation is relatively larger than the range of ±14.5 FNU. This study has discovered some potential errors in using the nighttime DNB data that, if

addressed, may serve usefully as a launching point for the future development of more accurate algorithms to calculate nighttime turbidity.

6. References

Anderson, C.W., 2005. Turbidity, in: Wilde F.D., Radtke D.B. (Eds.), Chapter A6. Field measurements: National Field Manual for the Collection of Water-Quality Data, USGS Office of Water Quality, 1-55.

Babin, M., Morel, A., Fournier-Sicre, V., Fell, F., & Stramski, D., 2003a. Light scattering properties of marine particles in coastal and open ocean waters as related to the particle mass concentration. Limnol. Oceanogr. 48, 843-859.

Babin, M., Stramski, D., Ferrari, G.M., Claustre, H., Bricaud, A., Obolensky, G., & Hoepffner, N., 2003b. Variations in the light absorption coefficients of phytoplankton, nonalgal particles, and dissolved organic matter in coastal waters around Europe. J. Geophys. Res. 108 (C7), 3211-3230.

Chen, S., Hu, C., 2017. Estimating sea surface salinity in the Northern Gulf of Mexico from satellite ocean color measurements. Remote Sens. Environ. 201, 115-132.

Chen, Z., Hu, C., Muller-Karger, F., 2007. Monitoring turbidity in Tampa Bay using MODIS/Aqua 250-m imagery. Remote Sens. Environ 109, 207-220.

CRCSI, 2017. Volume 1B: Data-Image interpretation, in: Harrison, B.A., Jupp, D.L.B., Lewis, M.M., Forster, B.C., Coppa, I., Mueller, N., Hudson, D., Phinn, S., Smith, C., Anstee, J., Grant, I., Dekker, A.G., Ong, C., and Lau, I. (Eds.), Earth Observation: Data, Processing and Applications. CRCSI, Melbourne.

Croft, T.A., 1978. Nighttime images of the earth from space. Sci. Am. 239 (1), 86-101.

Dogliotti, A.I., Ruddick, K., Nechad, B., Lasta, C., Mercado, A., Hozbor, M., Guerrero, R., Riviello López, G., Abelando, M., 2014. Calibration and validation of an algorithm for remote sensing of turbidity over La Plata River estuary, Argentina. EARSeL eProceedings, 10 (2), 119-130.

Dogliotti, A.I., Ruddick, K.G., Nechad, B., Doxaran, D., Knaeps, E., 2015. A single algorithm to retrieve turbidity from remotely-sensed data in all coastal and estuarine waters. Remote Sens. Environ. 156, 157-168.

Eastman, R., S.G. Warren, and C.J. Hahn, 2011. Variations in cloud cover and cloud types over the ocean from surface observations, 1954–2008. J. Climate, 24, 5914–5934.

Ellrod, G.P., 1995. Advances in the detection and analysis of fog at night using GOES multispectral infrared imagery. Wea. Forecasting. 10, 606-619.

Eyre, J.R., Brownscombe, J.L., Allam, R.J., 1984. Detection of fog at night using Adavance Very High Resolution Radiometer (AVHRR) imagery. Meteorol. Mag. 113, 266-271.

Gordon, H.R., Wang, M., 1994. Retrieval of water-leaving radiance and aerosol optical thickness over the oceans with SeaWiFS: a preliminary algorithm. Appl. Optics. 33 (3), 443-452.

Hellweger, F.L., Miller, W., Oshodi, K.S., 2007. Mapping turbidity in the Charles River, Boston using a high-resolution satellite. Environ. Monit. Assess. 132 (1-3), 311-320.

Hill, C.M., P.J. Fitzpatrick, J.H. Corbin, Y.H. Lau, and S.K. Bhate, 2010. Summertime precipitation regimes associated with the sea breeze and land breeze in Southern Mississippi and Eastern Louisiana. Wea. Forecasting, 25, 1755–1779.

Hillger, D., Seaman, C., Liang, C., Miller, S., Lindsey, D., Kopp, T., 2014. Suomi NPP VIIRS Imagery evaluation. J. Geophys. Res. Atmos., 119, 6440–6455.

Hu, C., Carder, K.L., Muller-Karger, F.E., 2000. Atmospheric correction of SeaWiFS imagery over turbid coastal waters: a practical method. Remote Sens. Environ. 74, 195-206.

Hunt, G.E., 1973. Radiative properties of terrestrial clouds at visible and infrared thermal window wavelengths. Quarterly Journal of the Royal Meteorological Society, 99, 346-369.

International Organization for Standardization (ISO), 1999. Water quality-determination of turbidity. ISO, 7027.

Jones, S.E., Jago, C.F., Bale, A.J., Chapman, D., Howland, R.J.M., Jackson, J., 1998. Aggregation and resuspension of suspended particulate matter at a seasonally stratified site in the southern North Sea: physical and biological controls. Cont. Shelf Res. 18 (11), 1283-1309.

Kanamitsu, M., Ebisuzaki, W., Woollen, J., Yang, S., Hnilo, J.J., Fiorino, M., Potter, G.L., 2002. NCEP–DOE AMIP-II Reanalysis (R-2). Bull. Amer. Meteor. Soc., 83, 1631–1644.

Koponen, S., Pulliainen, J., Kallio, K., Hallikainen, M., 2002. Lake water quality classification with airborne hyperspectral spectrometer and simulated MERIS data. Remote Sens. Environ. 79 (1), 51-59.

Lathrop Jr, R.G., Lillesand, T.M., 1986. Use of Thematic Mapper data to assess water quality in Green Bay and central Lake Michigan. Photogramm. Eng. Rem. S. 52 (5), 671-680.

Lee, T.E., Miller, S.D., Turk, F.J., Schueler, C., Julian, R., Deyo, S., Dills, P., Wang, S., 2006. The NPOESS VIIRS day/night visible sensor. Bull. Amer. Meteor. Soc. 87, 191-199.

Lee, T.F., Nelson, C.S., Dills, P., Riishojgaard, L.P., Jones, A., Li, L., Miller, S., Flynn, L.E., Jedlovec, G., McCarty, W., Hoffman, C., McWilliams, G., 2010. NPOESS: Next-Generation Operational Global Earth Observations. Bull. Amer. Meteor. Soc. 91, 727-740.

Matthews, M.W., 2011. A current review of empirical procedures of remote sensing in inland and near-coastal transitional waters. Int. J. Remote Sens. 32 (21), 6855-6899.

Miller, S.D., Straka, W., Mills, S., Elvidge, C., Lee, T., Solbrig, J., Walther, A., Heidinger, A., & Weiss, S., 2013. Illuminating the capabilities of the Suomi National Polar-Orbiting Partnership (NPP) visible infrared imaging radiometer suite (VIIRS) day/night band. Remote Sens. 5(12), 6717-6766.

Miller, S.D., Turner, R.E., 2009. A dynamic lunar spectral irradiance data set for NPOESS/VIIRS day/night band nighttime environmental applications. IEEE T. Geosci. Remote. 47 (7), 2316-2329.

Mobley, C., 1994. Light and Water: Radiative Transfer in Natural Waters. 1st ed. Academic Press.

Morel, A., Prieur, L., 1977. Analysis of variations in ocean color. Limnol. Oceanogr. 22 (4), 709-722.

National Geophysical Data Center, 2006. 2-minute Gridded Global Relief Data (ETOPO2) v2. National Geophysical Data Center, NOAA.

Navalgund, R., V, J., Roy, P., 2007. Remote sensing applications: an overview. Curr. Sci. India. 93 (12), 1747-1766.

Nechad, B., Ruddick, K.G., & Neukermans, G., 2009. Calibration and validation of a generic multisensor algorithm for mapping of turbidity in coastal waters. Proc. SPIE. 7473, 74730H.

Nechad, B., Ruddick, K.G., Park, Y., 2010. Calibration and validation of a generic multisensor algorithm for mapping of total suspended matter in turbid waters. Remote Sens. Environ. 114 (4), 854-866.

Neter, J., Wasserman, W., 1974. Applied Linear Statistical Models: Regression, Analysis of Variance, and Experimental Designs, first ed. Richard D. Irwin, Inc, Homewood, Illinois.

Omar, A. F., MatJafri, M.Z., 2009. Turbidimeter design and analysis: a review on optical fiber sensors for the measurement of water turbidity. Sensors. 9 (10), 8311-8335.

Pahlevan, N., Roger, J., Ahmad, Z., 2017. Revisiting short-wave-infrared (SWIR) bands for atmospheric correction in coastal waters. Opt. Express, 25 (6), 6015-6035.

Petus, C., Chust, G., Gohin, F., Doxaran, D., Froidefond, J.-M., Sagarminaga, Y., 2010. Estimating turbidity and total suspended matter in the Adour River plume (South Bay of Biscay) using MODIS 250-m imagery. Cont. Shelf Res. 30 (5), 379-392.

Rhinehart, R.R., 2016. Nonlinear Regression Modeling for Engineering Applications: Modeling, Model Validation, and Enabling Design of Experiments. First Ed. John Wiley & Sons, United Kingdom.

Rossow, W.B., Schiffer, R.A., 1999. Advances in Understanding Clouds from ISCCP. Bull. Amer. Meteor. Soc., 80, 2261–2288.

Schueler, C.F., Clement, J.E., Ardanuy, P.E., Welsch, C., DeLuccia, F., Swenson, H., 2002. NPOESS VIIRS sensor design overview. Proc. SPIE. 4483, 11-23.

Shi, W., & Wang, M., 2018. Ocean dynamics observed by VIIRS day/night band satellite observations. Remote Sens. 10 (1), 76.

Siegel, D., Wang, M., Maritorena, S., Robinson, W., 2000. Atmospheric correction of satellite ocean color imagery: the black pixel assumption. Appl. Opt. 39 (21), 3582-3591.

Sullivan, W.T., 1989. A 10 km resolution image of the entire night-time Earth based on cloud-free satellite photographs in the 400–1100 nm band. Int. J. Remote Sens. 10 (1), 1-5.

Vanhellemont, Q., Ruddick, K., 2015. Advantages of high quality SWIR bands for ocean colour processing: Examples from Landsat-8. Remote Sens. Environ. 161, 89-106.

Xin Q., Woodcock, C.E., Liu, J., Tan, B., Melloh, R.A., Davis R.E., 2012. View angle effects on MODIS snow mapping in forests. Remote Sens. Environ. 118, 50-59.

7. Tables

Table 1. Summary of monthly water pixel contribution. The table shows data on the Louisiana Shelf during the day and night, calculating valid water pixels in all images. The method is described in the equation (1) of the Research Methods Section.

Date	Number of Nighttime Pixels	Number of Daytime Pixels	DNB contribution (%)	Daytime contribution (%)
Jan-16	1688108	2638329	39.0	61.0
Feb-16	3535749	4955656	41.6	58.4
Mar-16	1313554	2586586	33.7	66.3
Apr-16	2196585	3413323	39.2	60.8
May-16	1700947	3851209	30.6	69.4
Jun-16	2200518	3578819	38.1	61.9
Jul-16	2245524	3891386	36.6	63.4
Aug-16	1379380	3114104	30.7	69.3
Sep-16	2154369	3763976	36.4	63.6
Oct-16	2437953	4888458	33.3	66.7
Nov-16	2078314	3502239	37.2	62.8
Dec-16	1986773	3119638	38.9	61.1
Jan-17	1703674	3498806	32.8	67.3
Feb-17	2128253	3872143	35.5	64.5
Mar-17	3252200	3442961	48.6	51.4
Apr-17	3902307	2341585	62.5	37.5
May-17	3710174	2637879	58.5	41.6
Jun-17	2216331	2170163	50.5	49.5
Jul-17	3194521	2401261	57.1	42.9
Aug-17	2353921	1735821	57.6	42.4
Sep-17	3737971	3898495	49.0	51.1
Oct-17	3238834	3464760	48.3	51.7
Nov-17	3664108	4525591	44.7	55.3
Dec-17	2592175	2622569	49.7	50.3

Table 2. Summary of turbidity events (2016-2017). The table shows the turbidity events found during 2016 and 2017. The columns from the left to right indicate date, GMT time, turbidity pattern, and moon phase as days within the full moon. “y” = yes and “y/n” = maybe. The last column from the right shows where the turbidity pattern was found. “afa” = Atchafalaya Bay, “miss” = Mississippi River Delta, and “afa+miss”=both regions. In summary, there are 86 “y” cases and 47 “y/n” cases.

Date	GMT	Turbidity Pattern	Moon Phase	Region
20160121	0749	y/n	Full Moon - 2	afa
20160123	0851	y	Full Moon	afa
20160123	0714	y	Full Moon	afa+miss
20160124	0651	y	Full Moon + 1	afa+miss
20160124	0833	y	Full Moon + 1	afa+miss
20160129	0700	y	Full Moon + 4	afa+miss
20160212	0740	y/n	Full Moon - 10	miss
20160214	0659	y/n	Full Moon - 8	miss
20160216	0801	y/n	Full Moon - 6	miss
20160220	0827	y/n	Full Moon - 2	afa+miss
20160223	0729	y/n	Full Moon + 1	miss
20160224	0712	y/n	Full Moon + 2	miss
20160225	0654	y	Full Moon + 3	afa+miss
20160225	0831	y	Full Moon + 3	afa+miss
20160226	0813	y	Full Moon + 4	afa+miss
20160227	0756	y	Full Moon + 5	afa
20160228	0738	y	Full Moon + 6	afa
20160321	0723	y	Full Moon - 2	afa+miss
20160322	0843	y	Full Moon - 1	afa
20160322	0706	y	Full Moon - 1	afa+miss
20160323	0825	y/n	Full Moon	afa
20160324	0808	y	Full Moon + 1	afa
20160325	0750	y	Full Moon + 2	afa+miss
20160421	0744	y	Full Moon - 1	miss
20160423	0703	y	Full Moon + 1	afa+miss
20160423	0846	y	Full Moon + 1	afa
20160424	0646	y	Full Moon + 2	afa+miss
20160426	0748	y	Full Moon + 4	afa+miss
20160427	0730	y	Full Moon + 5	miss
20160521	0822	y	Full Moon	afa
20160523	0742	y	Full Moon + 2	miss
20160524	0724	y	Full Moon + 3	miss

Table 2. (Continued). Summary of valid cases.

Date	GMT	Turbidity Pattern	Moon Phase	Region
20160620	0718	y	Full Moon	miss
20160621	0701	y	Full Moon + 1	miss
20160621	0838	y	Full Moon + 1	miss
20160622	0820	y	Full Moon + 2	afa
20160623	0803	y	Full Moon + 3	miss
20160624	0745	y/n	Full Moon + 4	afa+miss
20160625	0722	y	Full Moon + 5	afa+miss
20160626	0704	y/n	Full Moon + 6	afa
20160719	0814	y/n	Full Moon	afa+miss
20160721	0739	y/n	Full Moon + 2	afa+miss
20160814	0643	y/n	Full Moon - 4	miss
20160818	0710	y	Full Moon	miss
20160819	0835	y/n	Full Moon + 1	afa+miss
20160820	0812	y/n	Full Moon + 2	afa+miss
20160821	0754	y	Full Moon + 3	afa
20160822	0737	y	Full Moon + 4	afa
20160824	0656	y/n	Full Moon + 6	afa
20160915	0823	y	Full Moon - 1	afa
20160916	0806	y/n	Full Moon	afa+miss
20160918	0731	y	Full Moon + 2	afa
20160919	0713	y	Full Moon + 3	afa
20160919	0850	y	Full Moon + 3	afa
20160920	0650	y/n	Full Moon + 4	afa
20160920	0833	y	Full Moon + 4	afa
20161014	0742	y	Full Moon - 2	afa
20161015	0725	y	Full Moon - 1	afa
20161016	0707	y	Full Moon	afa
20161016	0844	y	Full Moon	afa
20161017	0644	y	Full Moon + 1	afa
20161018	0809	y	Full Moon + 2	afa
20161020	0728	y/n	Full Moon + 4	afa+miss
20161114	0803	y	Full Moon	afa
20161117	0705	y	Full Moon + 3	afa
20161117	0847	y	Full Moon + 3	afa
20161211	0757	y	Full Moon - 2	afa

Table 2. (Continued). Summary of valid cases.

Date	GMT	Turbidity Pattern	Moon Phase	Region
20170110	0830	y/n	Full Moon - 2	afa
20170111	0812	y	Full Moon - 1	afa+miss
20170114	0714	y/n	Full Moon + 2	afa+miss
20170114	0720	y	Full Moon + 2	afa+miss
20170116	0822	y/n	Full Moon + 4	miss
20170210	0851	y	Full Moon - 1	afa
20170210	0708	y	Full Moon - 1	afa+miss
20170211	0651	y	Full Moon	miss
20170211	0833	y	Full Moon	miss
20170212	0816	y	Full Moon + 1	miss
20170213	0753	y/n	Full Moon + 2	miss
20170214	0735	y/n	Full Moon + 3	afa+miss
20170216	0700	y/n	Full Moon + 4	afa+miss
20170216	0837	y/n	Full Moon + 4	afa+miss
20170315	0654	y	Full Moon + 3	afa+miss
20170316	0813	y	Full Moon + 4	afa+miss
20170317	0756	y	Full Moon + 5	afa+miss
20170407	0758	y	Full Moon - 4	afa
20170408	0741	y	Full Moon - 3	afa+miss
20170409	0723	y	Full Moon - 2	afa+miss
20170411	0643	y/n	Full Moon	miss
20170411	0825	y/n	Full Moon	miss
20170413	0750	y	Full Moon + 2	afa+miss
20170507	0700	Y	Full Moon - 3	miss
20170508	0819	y	Full Moon - 2	afa
20170509	0802	y	Full Moon - 1	miss
20170510	0744	y	Full Moon	miss
20170511	0721	y/n	Full Moon + 1	miss
20170512	0703	y/n	Full Moon + 2	miss
20170512	0846	y/n	Full Moon + 2	afa
20170513	0646	y	Full Moon + 3	afa
20170513	0828	y	Full Moon + 3	afa
20170514	0805	y	Full Moon + 4	afa+miss
20170515	0748	y	Full Moon + 5	afa+miss
20170516	0730	y	Full Moon + 6	afa+miss

Table 2. (Continued). Summary of valid cases.

Date	GMT	Turbidity Pattern	Moon Phase	Region
20170608	0657	y	Full Moon - 1	afa+miss
20170609	0640	y/n	Full Moon	miss
20170609	0817	y	Full Moon	afa+miss
20170610	0759	y	Full Moon + 1	afa+miss
20170611	0742	y/n	Full Moon + 2	miss
20170706	0811	y/n	Full Moon - 3	afa
20170707	0753	y/n	Full Moon - 2	afa+miss
20170708	0736	y/n	Full Moon - 1	afa+miss
20170709	0718	y	Full Moon	afa+miss
20170710	0837	y/n	Full Moon + 1	afa
20170710	0655	y/n	Full Moon + 1	afa
20170711	0638	y/n	Full Moon + 2	miss
20170712	0802	y/n	Full Moon + 3	afa+miss
20170807	0814	y/n	Full Moon	afa+miss
20170808	0757	y/n	Full Moon + 1	miss
20170904	0751	y/n	Full Moon - 2	afa+miss
20170909	0754	Y	Full Moon + 3	afa+miss
20170911	0719	Y	Full Moon + 5	afa+miss
20171004	0646	y/n	Full Moon - 1	afa+miss
20171004	0829	y	Full Moon - 1	afa
20171005	0806	y	Full Moon	afa
20171006	0748	y	Full Moon + 1	afa
20171102	0742	y	Full Moon - 2	afa+miss
20171104	0707	y/n	Full Moon	afa
20171105	0644	y/n	Full Moon + 1	afa
20171105	0827	y	Full Moon + 1	afa
20171106	0809	y	Full Moon + 2	afa
20171202	0821	y	Full Moon - 1	afa
20171209	0749	y	Full Moon + 6	afa
20171230	0757	y/n	Full Moon - 2	miss

Table 3. Summary of monthly water pixel contribution (selected DNB cases). The table shows water turbidity estimation in the Northern Gulf of Mexico (**Figure 1**) during day and night. The nighttime DNB contribution is calculated from water pixels in the turbidity events ("y" cases in **Table 2**)**,** while the daytime contribution is calculated from the images in the whole month.

Date	Number of Nighttime Pixels	Number of Daytime Pixels	DNB contribution (%)	Daytime contribution (%)
Jan-16	512464	2638329	16.3	83.7
Feb-16	1323154	4955656	21.1	78.9
Mar-16	369593	2282399	13.9	86.1
Apr-16	561606	2171977	20.5	79.5
May-16	322044	2460259	11.6	88.4
Jun-16	1237105	2350822	34.5	65.5
Jul-16	146808	2644432	5.26	94.7
Aug-16	469256	1963712	19.3	80.7
Sep-16	266974	2604340	9.30	90.7
Oct-16	533395	4717491	10.2	89.8
Nov-16	244933	3497088	6.55	93.5
Dec-16	87430	3119638	2.73	97.3
Jan-17	265630	3498806	7.06	92.9
Feb-17	512811	3448969	12.9	87.1
Mar-17	571579	3389153	14.4	85.6
Apr-17	988968	2304195	30.0	70.0
May-17	1718462	2589241	39.9	60.1
Jun-17	675337	2156190	23.9	76.2
Jul-17	836338	2384574	26.0	74.0
Aug-17	205875	1673773	11.0	89.1
Sep-17	234489	3886430	5.69	94.3
Oct-17	334585	3413968	8.93	91.1
Nov-17	696019	4456592	13.5	86.5
Dec-17	270265	2582639	9.47	90.5

Table 4. Summary of monthly water pixel contribution (Full moon ±4 days) in estimating turbid pixels. The data counts the water pixels in the turbidity events ("y" cases in **Table 2**). Both the DNB contribution and the daytime contribution were calculated within ± 4 days of full moon.

Date	Number of Nighttime Pixels	Number of Daytime Pixels	DNB contribution (%)	Daytime contribution (%)
Jan-16	512464	852997	37.5	62.5
Feb-16	607471	1675218	26.6	73.4
Mar-16	369593	403896	47.8	52.2
Apr-16	438515	991644	30.7	69.3
May-16	322044	240672	57.2	42.8
Jun-16	933133	915631	50.5	49.5
Jul-16	146808	698351	17.4	82.6
Aug-16	433479	937478	31.6	68.4
Sep-16	266974	962866	21.7	78.3
Oct-16	533395	2109773	20.2	79.8
Nov-16	244933	1304242	15.8	84.2
Dec-16	87430	1296960	6.32	93.7
Jan-17	265630	1231015	17.8	82.3
Feb-17	512811	1332439	27.8	72.2
Mar-17	398497	912338	30.4	69.6
Apr-17	988968	721793	57.8	42.2
May-17	1385432	1408683	49.3	50.4
Jun-17	675337	937914	41.7	58.1
Jul-17	836338	932863	47.3	52.7
Aug-17	205875	445260	31.6	68.4
Sep-17	172707	738242	19.0	81.0
Oct-17	334585	511104	39.6	60.4
Nov-17	696019	1538397	31.2	68.9
Dec-17	256303	887265	22.4	77.6

Table 5. Summary of the four different equations in **Figure 16**. See Research Methods Section for details.

	Equation 1	Equation 2	Equation 3	Equation 4
Standard Error (FNU)	7.42	7.34	7.36	7.45
R^2	0.61	0.61	0.61	0.60
Adjusted R^2	0.61	0.61	0.61	0.60
Residual Variance	55.06	53.97	54.10	55.47
Reduced Chi-square (13.7%)	153.5	340.1	217.6	213.4
Reduced Chi-square (22%)	59.53	131.9	84.39	82.77
Mean Relative Bias (%)	53.5	76.4	63.1	66.2
Mean Relative Error (%)	82.3	101.8	90.1	91.4

Table 6. Summary statistics of the four equations used to fit data. The standard error of the predicted nighttime turbidity, lower limit, and upper limit of the 95% prediction interval are shown in **Figure 16**. See Research Methods Section for details.

	DNB Reflectance (Unitless)	Mean Daytime Turbidity (FNU)	Standard Deviation of Daytime Turbidity (FNU)	Number of Daytime Turbid Pixels	Predicted Nighttime Turbidity (FNU)	Standard Error of the Predicted Nighttime Turbidity (FNU)	Lower Limit of the 95% Prediction Interval (FNU)	Upper Limit of the 95% Prediction Interval (FNU
Equation 1	0.02	6.42	4.180	33541	6.87	4.075	0	21.39
	0.04	14.6	6.901	27037	15.4	6.828	0.8584	29.92
	0.06	27.3	14.06	14660	24.7	14.17	10.13	39.20
	0.08	32.3	10.77	3442	34.5	10.72	19.93	49.02
	0.10	39.3	7.459	748	44.7	9.268	30.17	59.27
Equation 2	0.02	6.42	4.180	33541	6.27	4.049	0	20.65
	0.04	14.6	6.901	27037	14.9	6.812	0.4767	29.26
	0.06	27.3	14.06	14660	26.3	13.92	11.94	40.73
	0.08	32.3	10.77	3442	34.9	10.89	20.49	49.29
	0.10	39.3	7.459	748	38.9	7.487	24.51	53.32
Equation 3	0.02	6.42	4.180	33541	6.29	4.047	0	20.68
	0.04	14.6	6.901	27037	15.30	6.824	0.8949	29.71
	0.06	27.3	14.06	14660	25.67	14.00	11.26	40.07
	0.08	32.3	10.77	3442	34.68	10.80	20.27	49.09
	0.10	39.3	7.459	748	41.32	7.719	26.91	55.75
Equation 4	0.02	6.42	4.180	33541	7.399	4.165	0	21.97
	0.04	14.6	6.901	27037	15.47	6.835	0.8779	30.05
	0.06	27.3	14.06	14660	24.30	14.25	9.706	38.89
	0.08	32.3	10.77	3442	34.00	10.65	19.41	48.60
	0.10	39.3	7.459	748	44.72	9.253	30.15	59.35

** Nighttime DNB reflectance was given at five difference values: 0.02-0.1*

** Mean daytime turbidity was calculated from the daytime turbidity maps in the 53 usable cases at the given nighttime DNB reflectance value. For example, when nighttime DNB reflectance = 0.02, there are 33541 turbid pixels from the 53 events to calculate the mean daytime turbidity.*

** Standard deviation of daytime turbidity was calculated from the daytime turbidity maps in the 53 usable cases at the given nighttime DNB reflectance.*

** Number of daytime turbid pixels was obtained from the daytime turbidity maps in the 53 usable cases at the given nighttime DNB reflectance.*

** Predicted nighttime turbidity was derived from the equation at the given nighttime DNB reflectance in the first column.*

** Standard error of the predicted nighttime turbidity was calculated using the equation (13) in the Research Methods Section.*

** Lower limit and upper limit of the 95% prediction interval were calculated from the equation (17) & (18) in the Research Methods Section.*

Table 7. Summary statistics of 53 valid cases with mean relative bias and error. See Research Methods Section for details.

Date	GMT	DNB Reflectance (Unitless)				Day Turbidity (FNU)				Predicted Turbidity (FNU)				Mean Relative Bias (%)	Mean Relative Error (%)
		Min	Max	Mean	STD	Min	Max	Mean	STD	Min	Max	Mean	STD		
20160123	0714	0.0023	0.0672	0.0348	0.0187	4.99	57.28	23.95	15.21	0.56	28.16	13.47	8.09	-45.10	45.10
20160124	0833	0.0016	0.091	0.0463	0.0258	3.55	38.09	16.20	8.87	0.37	40.07	18.86	11.66	6.40	27.50
20160225	0831	0.0022	0.0633	0.0328	0.0176	6.72	54.05	26.99	16.37	0.54	26.25	12.57	7.53	-54.80	54.80
20160226	0813	0.0019	0.0716	0.0368	0.0201	5.01	55.67	19.36	15.69	0.44	30.32	14.39	8.77	-20.60	28.30
20160227	0756	0.0015	0.0651	0.0333	0.0184	2.54	52.37	16.11	12.64	0.33	27.14	12.83	7.87	-17.30	17.30
20160228	0738	0.0027	0.076	0.0394	0.0211	1.89	52.64	10.75	11.47	0.68	32.46	15.56	9.31	81.30	89.60
20160325	0750	0.0011	0.0827	0.0419	0.0236	0.95	44.25	14.58	11.09	0.24	35.83	16.79	10.46	17.10	26.60
20160423	0703	0.0022	0.07	0.0361	0.0196	3.00	58.75	23.68	20.29	0.53	29.54	14.09	8.50	-19.10	37.40
20160622	0820	0.0022	0.0592	0.0307	0.0165	1.02	25.88	7.17	5.35	0.52	24.29	11.64	6.97	70.80	72.60
20160915	0823	0.0024	0.061	0.0317	0.0169	5.10	28.01	16.64	6.47	0.58	25.14	12.08	7.20	-35.00	35.00
20160919	0713	0.0021	0.0557	0.0289	0.0155	2.38	25.40	10.46	6.56	0.50	22.63	10.86	6.49	1.90	15.10
20160920	0833	0.0023	0.0622	0.0323	0.0173	0.75	18.55	7.33	5.74	0.56	25.74	12.35	7.38	99.80	100.20
20161016	0707	0.0019	0.0374	0.0197	0.0103	2.06	17.62	8.08	4.73	0.44	14.25	6.92	4.04	-17.70	17.70
20161018	0809	0.0014	0.0542	0.0278	0.0153	1.73	26.90	12.00	6.88	0.32	21.93	10.41	6.34	-18.40	18.40
20161114	0803	0.0011	0.0436	0.0224	0.0123	1.72	18.69	10.38	5.63	0.25	17.01	8.07	4.92	-26.80	26.80
20161117	0705	0.0024	0.0451	0.0237	0.0123	1.10	14.20	5.95	4.11	0.58	17.68	8.62	5.00	58.50	60.70
20161211	0757	0.0019	0.043	0.0225	0.0119	3.67	40.18	16.20	11.32	0.45	16.76	8.10	4.77	-47.70	47.70
20170111	0812	0.0014	0.0287	0.0151	0.0079	3.97	33.17	13.93	7.67	0.31	10.48	5.08	2.98	-65.50	65.50
20170114	0720	0.0016	0.043	0.0223	0.012	2.16	23.21	11.46	5.84	0.35	16.76	8.03	4.81	-35.70	35.70
20170210	0708	0.0016	0.0511	0.0264	0.0143	4.64	17.32	10.89	4.00	0.36	20.47	9.76	5.89	-19.80	24.40
20170316	0813	0.0017	0.0615	0.0316	0.0173	1.29	33.24	10.53	8.29	0.38	25.40	12.06	7.34	28.10	35.80
20170317	0756	0.0033	0.0701	0.0367	0.0193	1.59	54.57	15.59	14.57	0.85	29.57	14.32	8.41	17.00	32.50
20170407	0758	0.0042	0.071	0.0376	0.0193	3.84	41.81	14.12	9.46	1.12	30.00	14.71	8.44	4.60	21.80
20170413	0750	0.0043	0.0431	0.0237	0.0112	2.66	31.62	11.36	7.09	1.16	16.79	8.57	4.56	-22.80	22.80
20170508	0819	0.0039	0.0969	0.0504	0.0269	0.86	53.70	18.72	18.52	1.01	43.06	20.71	12.32	95.40	107.00
20170514	0805	0.0033	0.0739	0.0386	0.0204	1.75	35.55	10.03	8.37	0.85	31.43	15.20	8.95	70.60	73.70
20170609	0817	0.0035	0.0723	0.0379	0.0199	1.41	43.25	17.28	13.60	0.91	30.63	14.86	8.70	5.70	26.20
20170610	0759	0.0011	0.0682	0.0347	0.0194	0.64	62.45	20.98	19.72	0.24	28.62	13.45	8.34	5.20	46.30
20170909	0754	0.0018	0.0386	0.0202	0.0106	2.38	17.56	8.93	4.48	0.41	14.79	7.16	4.21	-26.00	26.00
20170911	0719	0.0029	0.0624	0.0327	0.0172	6.75	24.26	14.13	5.36	0.74	25.81	12.51	7.34	-19.90	21.60
20171005	0806	0.0036	0.0414	0.0225	0.0109	5.96	29.62	15.59	7.47	0.93	16.02	8.07	4.40	-51.00	51.00
20171105	0827	0.0014	0.0424	0.0219	0.0118	0.69	19.35	9.21	6.00	0.31	16.47	7.87	4.74	-10.40	13.90
20171106	0809	0.0013	0.0445	0.0229	0.0125	0.96	24.40	9.11	6.33	0.29	17.43	8.30	5.02	-5.80	15.80
20171209	0749	0.0036	0.0878	0.0457	0.0243	4.12	39.45	16.01	9.27	0.94	38.40	18.49	10.97	9.40	22.10

** List of 34 cases in the Atchafalaya Bay*

Table 7. (Continued). Summary of 53 valid cases with mean relative bias and uncertainty.

Date	GMT	DNB Reflectance (dimensionless)				Day Turbidity (FNU)				Predicted Turbidity (FNU)				Mean Relative Bias (%)	Mean Relative Error (%)
		Min	Max	Mean	STD	Min	Max	Mean	STD	Min	Max	Mean	STD		
20160123	0714	0.0023	0.0543	0.0283	0.015	8.60	29.47	16.10	5.15	0.56	21.95	10.59	6.27	-40.40	40.40
20160129	0700	0.0059	0.1187	0.0623	0.0326	1.45	52.12	17.41	17.85	1.65	54.56	26.49	15.48	142.90	143.10
20160226	0813	0.0027	0.0803	0.0415	0.0224	0.88	37.34	12.03	11.09	0.67	34.64	16.56	9.96	115.40	116.30
20160227	0756	0.0018	0.0601	0.031	0.0168	0.96	36.22	10.41	9.55	0.42	24.74	11.78	7.13	63.60	71.40
20160228	0738	0.0022	0.0704	0.0363	0.0197	1.05	21.90	7.09	5.67	0.54	29.71	14.17	8.55	137.30	138.60
20160621	0701	0.0022	0.0747	0.0384	0.0209	0.38	22.16	8.07	6.29	0.52	31.83	15.15	9.18	137.00	137.00
20161117	0705	0.0017	0.0394	0.0205	0.0109	0.10	8.97	2.84	2.52	0.38	15.13	7.30	4.32	273.10	273.10
20161216	0801	0.0019	0.0547	0.0283	0.0152	1.43	23.42	7.13	6.08	0.43	22.14	10.59	6.36	63.50	69.10
20170114	0720	0.0009	0.084	0.0425	0.024	0.85	52.36	20.35	14.18	0.19	36.51	17.06	10.68	-14.00	14.50
20170210	0708	0.0013	0.0568	0.0291	0.016	0.18	60.08	16.99	17.32	0.30	23.16	10.96	6.71	29.90	65.20
20170316	0813	0.0034	0.0835	0.0435	0.0231	0.09	28.53	9.61	8.91	0.88	36.25	17.45	10.36	369.10	369.10
20170413	0750	0.0007	0.0414	0.0211	0.0117	0.14	9.68	3.57	2.49	0.15	16.02	7.54	4.66	160.40	160.40
20170507	0700	0.0047	0.1128	0.0588	0.0312	1.16	36.86	12.24	11.77	1.27	51.44	24.78	14.69	200.00	200.00
20170509	0802	0.0016	0.0669	0.0343	0.0188	0.12	47.91	14.30	15.08	0.37	28.00	13.26	8.11	94.90	113.60
20170608	0657	0.002	0.0696	0.0358	0.0195	0.12	29.57	8.46	9.14	0.49	29.30	13.95	8.45	433.30	433.40
20170909	0754	0.0017	0.0389	0.0203	0.0107	0.25	10.66	3.1	3.33	0.39	14.89	7.19	4.25	363.5	363.5
20170911	0719	0.0027	0.0691	0.0359	0.0192	0.28	23.07	8.56	7.34	0.68	29.08	13.98	8.32	191.0	191.0
20171102	0742	0.0014	0.0378	0.0196	0.0105	0.17	10.33	3.93	3.38	0.3	14.43	6.91	4.14	214.2	214.2
20171106	0809	0.0013	0.0277	0.0145	0.0076	0.17	7.51	2.77	2.28	0.27	10.05	4.86	2.86	132.2	132.2

** List of 19 cases in the Mississippi River Delta*

8. Figures

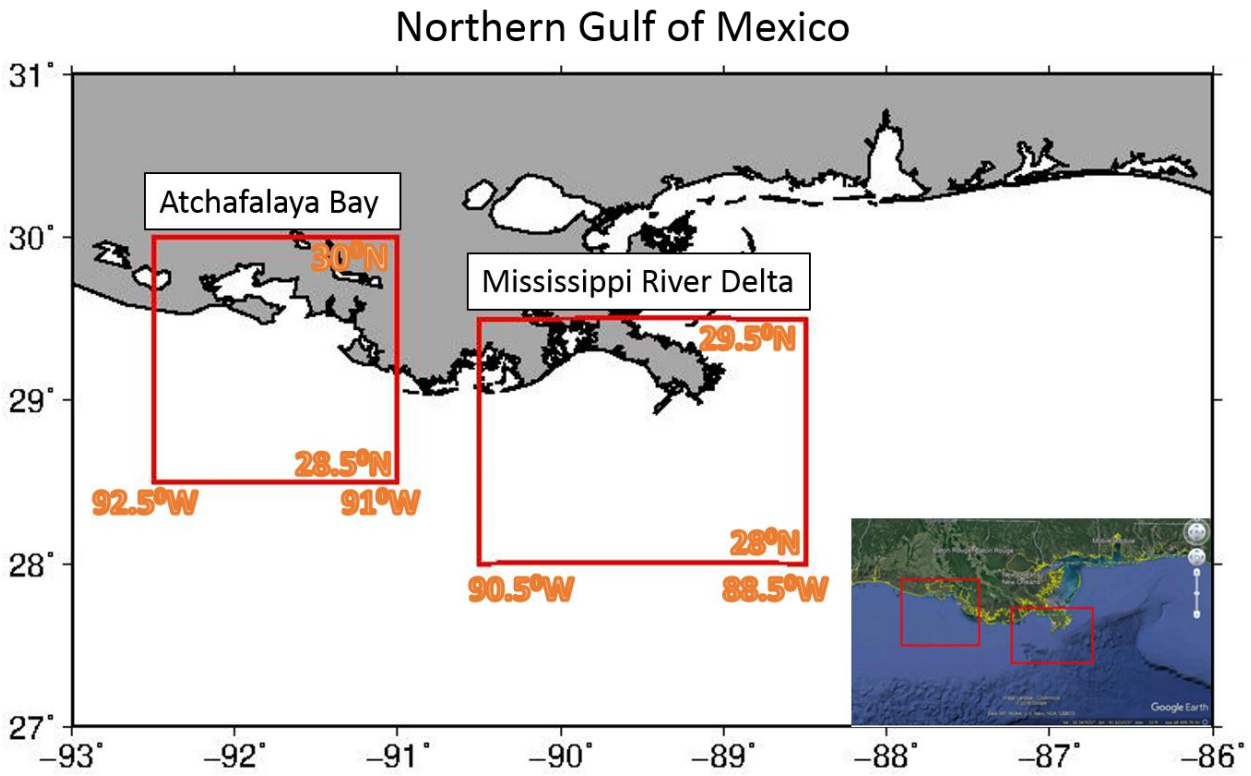

Figure 1. The two study regions shown in the Northern Gulf of Mexico and as an inset from Google Earth, which displays land and bathymetry of the Gulf of Mexico. The region shown in the left red box is defined by 91º - 92.5ºW and 28.5º - 30ºN while the other study region is defined 88.5º - 90.5ºW and 28º - 29.5ºN, which encompass the river mouths of the Atchafalaya Bay and Mississippi River Delta, respectively.

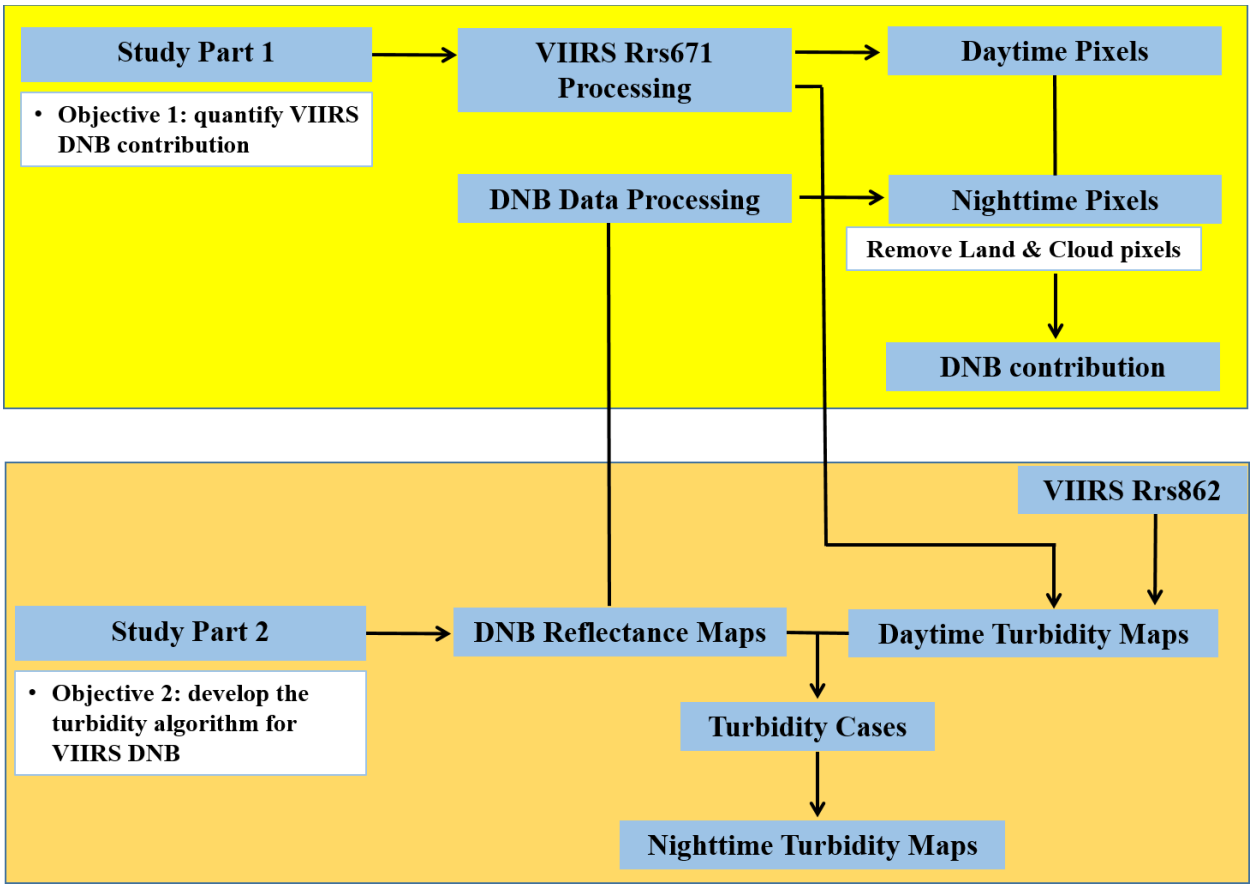

Figure 2. The overall flow chart for systematic data processing and analysis. See Research Methods Section for details.

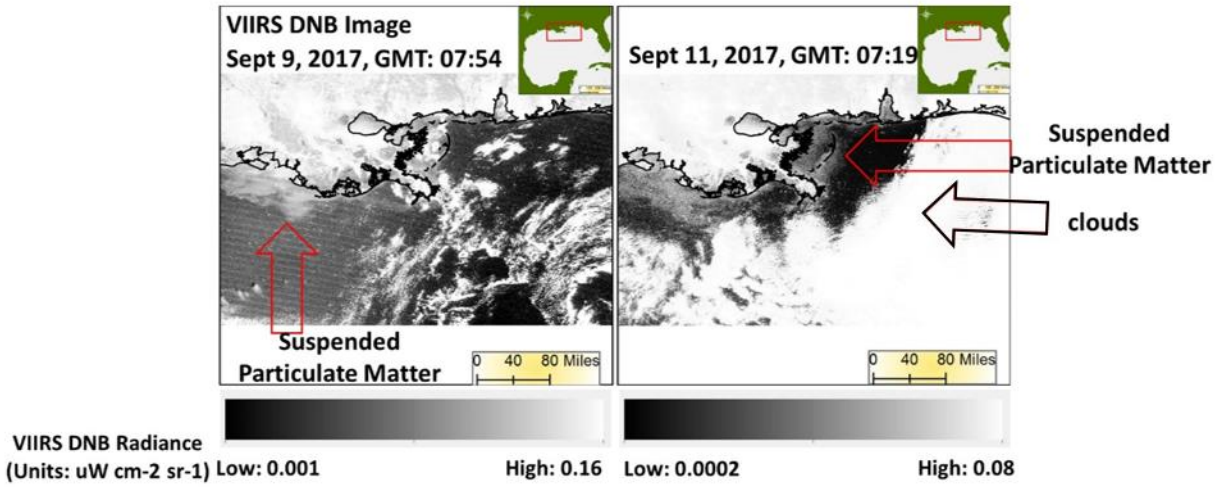

Figure 3. VIIRS nighttime DNB radiance maps in the Northern Gulf of Mexico. The two example images show turbidity events, as indicated via red arrows, in the Atchafalaya Bay and Mississippi River Delta on September 9 and 11, 2017. The nighttime DNB radiance maps show the examples before the land and cloud mask.

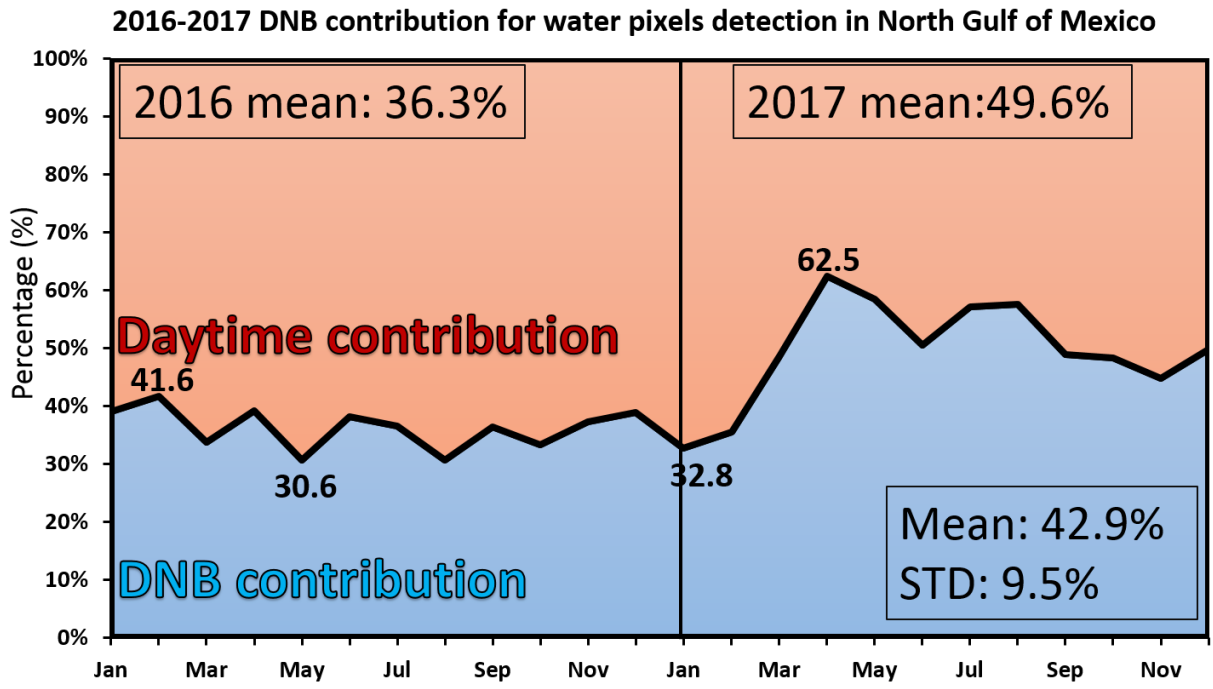

Figure 4. A monthly time-series plot of **Table 1**. The blue region represents the nighttime DNB water pixel contribution and the orange region is the daytime water pixel contribution. The X-axis is month of the year and Y-axis is percentage. The black line separates 2016 and 2017. The mean nighttime DNB contribution is 36.3% in 2016 and 49.6% in 2017. From 2016 to 2017, the mean nighttime DNB contribution is 42.9% and the standard deviation is 9.5%.

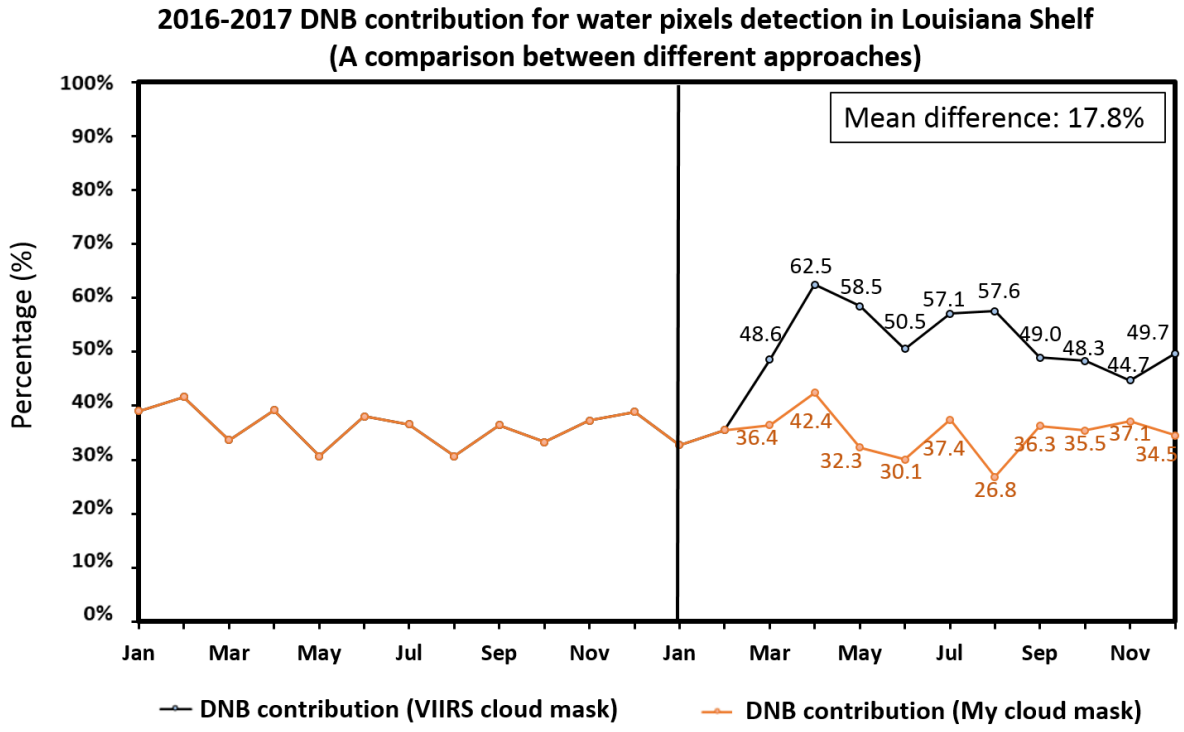

Figure 5. A comparison between the two cloud masking methods. The orange line indicates the nighttime DNB contribution using the cloud masking developed in this study, while the black line is using VIIRS cloud mask data. After March 2016, the mean difference shows that DNB contribution was underestimated about 17.8% through my cloud mask algorithm.

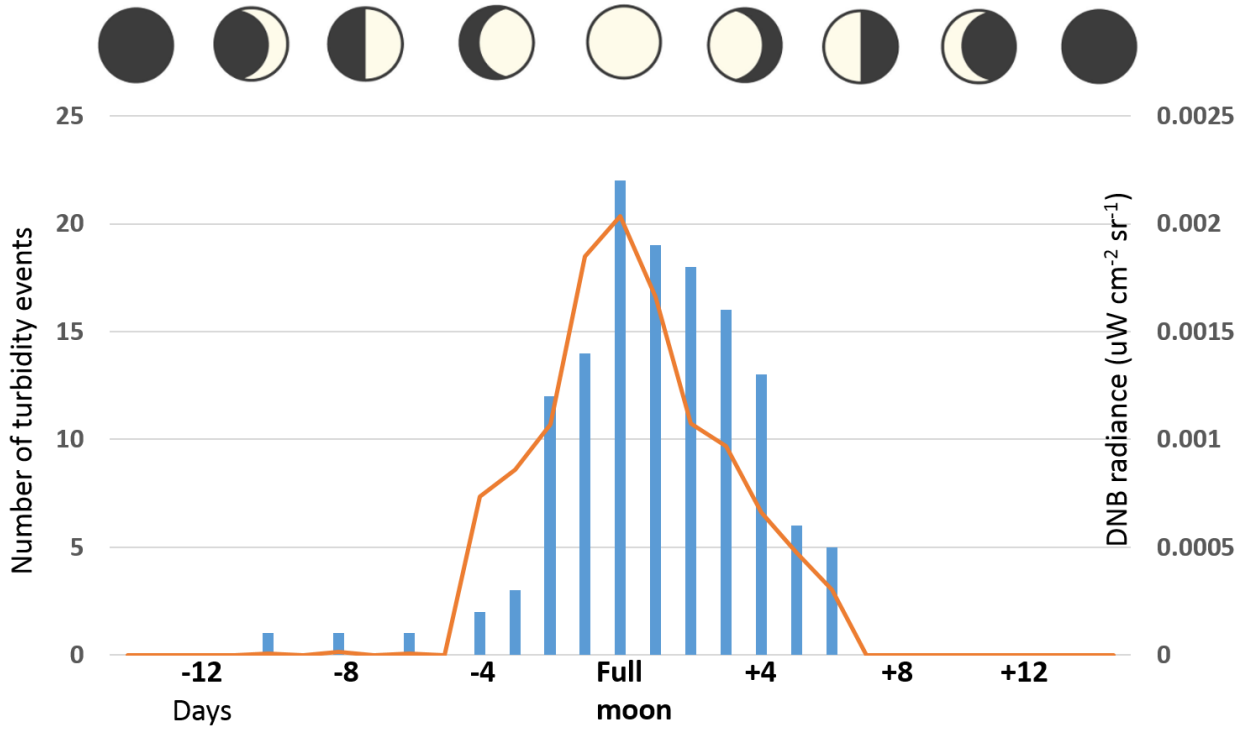

Figure 6. A plot from data in **Table 2**. The X-axis shows the number of days before or after the full moon. The two Y-axes are the number if turbidity events and nighttime DNB radiance, corresponding to the blue bars and orange line, respectively. The nighttime DNB radiance was calculated from the average of DNB mapped radiance in the turbidity events in the Northern Gulf of Mexico.

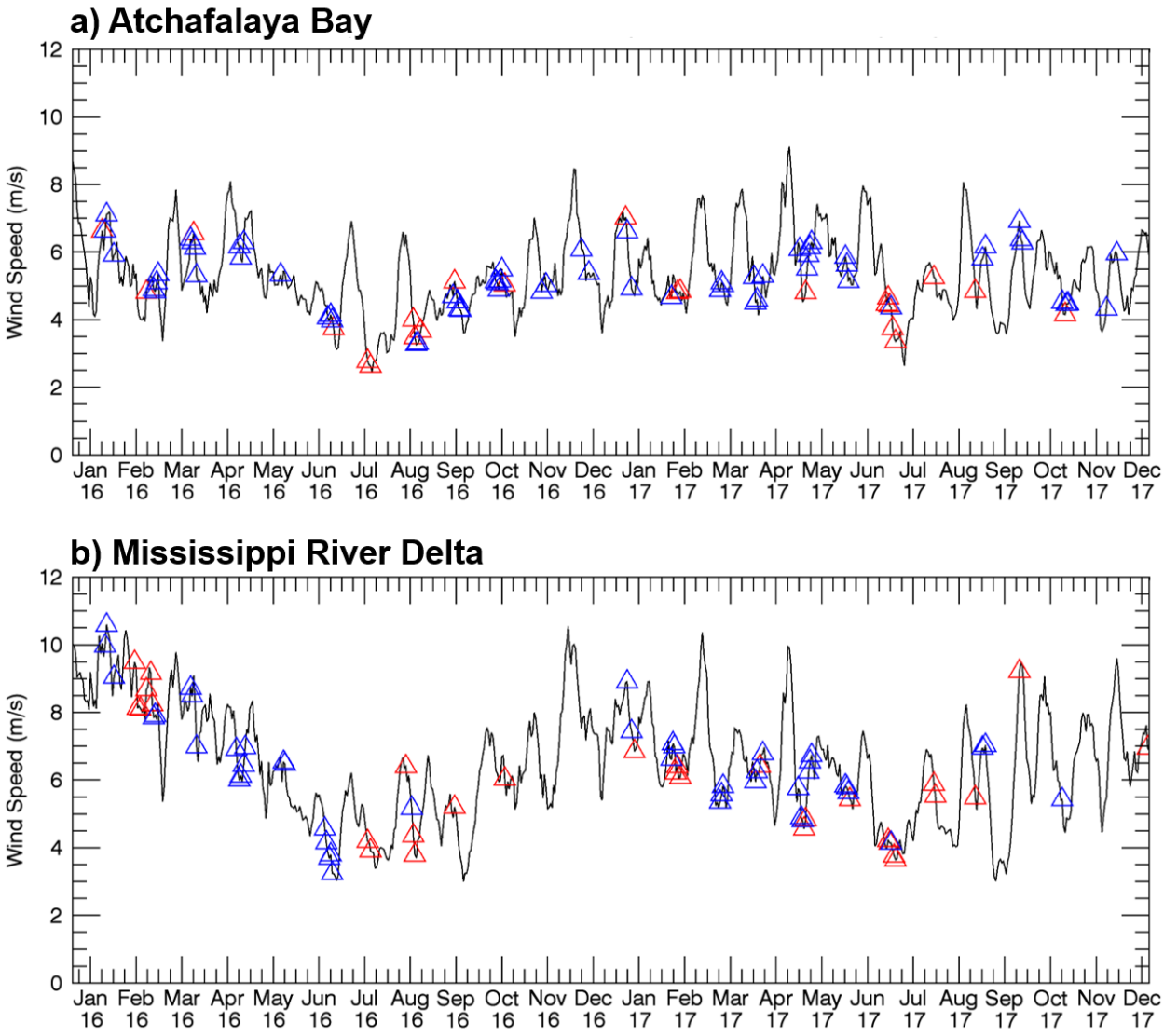

Figure 7. 2016-2017 time series of wind speed in the study regions. (a) and (b) show the records in the Atchafalaya Bay and the Mississippi River Delta, respectively. The black line indicates the variation of wind speed during 2016 and 2017. The wind speed data are from National Data Buoy Center and already smoothed with a boxcar average of 9 points. The triangle symbols mark all turbidity events in **Table 2**, according to their regions. The “y” cases are indicated in blue color and the “y/n” cases are in red.

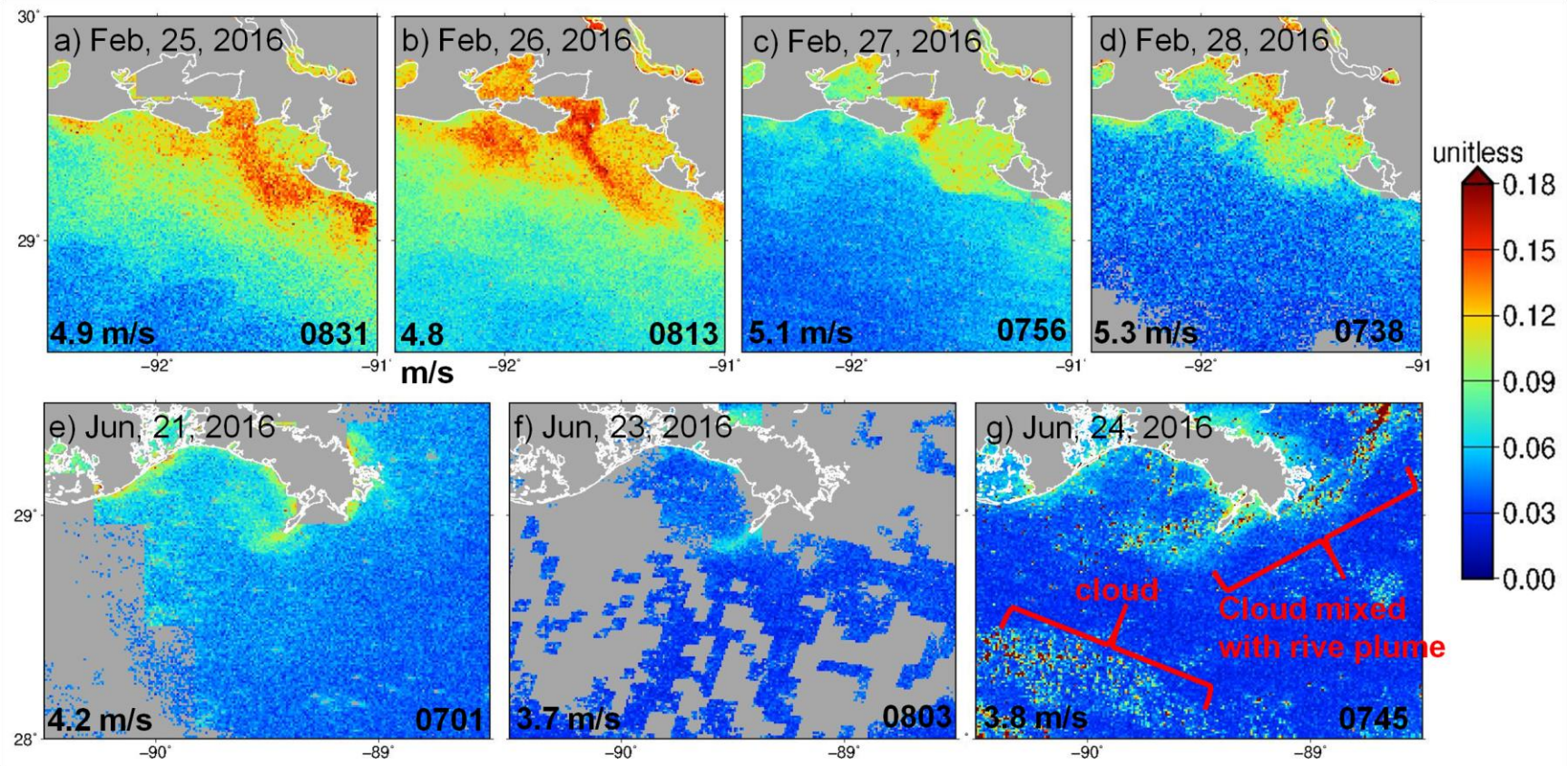

Figure 8. Selected VIIRS nighttime DNB reflectance maps for wind analysis. The cases were selected in the Atchafalaya Bay and the Mississippi River Delta. (a)~ (d) are four consecutive figures in the Atchafalaya Bay from February 25 to 27, 2016. (e) ~ (g) are in the Mississippi River Delta from June 21 to 24, 2016. The GMT time is labeled in the bottom right corner of each panel. The unit of nighttime DNB reflectance is dimensionless. The corresponding wind speeds provided by National Data Buoy Center are annotated in the bottom left corner of each panel. In these 7 panels, turbidity patterns are greenish and light reddish. In (g), this map did not have the cloud mask because of the step of box sieving in my algorithm, which masked the entire map. Some cloud pixels are remained and indicated as the dark red color while turbidity patterns are greenish. (g) is a typical “y/n” case listed in **Table 2**.

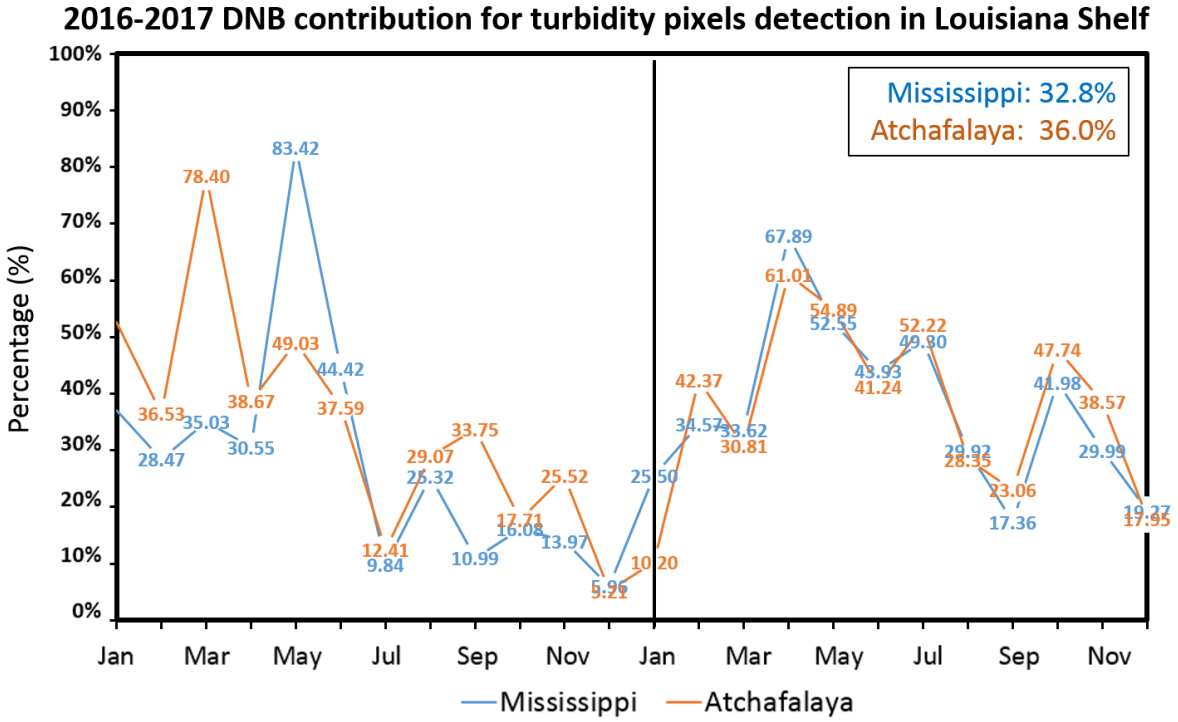

Figure 9. Monthly mean water pixels contribution for turbidity estimation. The data counts the valid water pixels in the nighttime DNB reflectance maps and daytime Rrs(671) maps from the turbidity events. The data are from **Table 4**, and separated into the two study regions. The blue line indicates the Mississippi River Delta and the orange line is the Atchafalaya Bay. The mean nighttime DNB contribution is 32.8% in the Mississippi River Delta and 36.0% in the Atchafalaya Bay during 2016 and 2017.

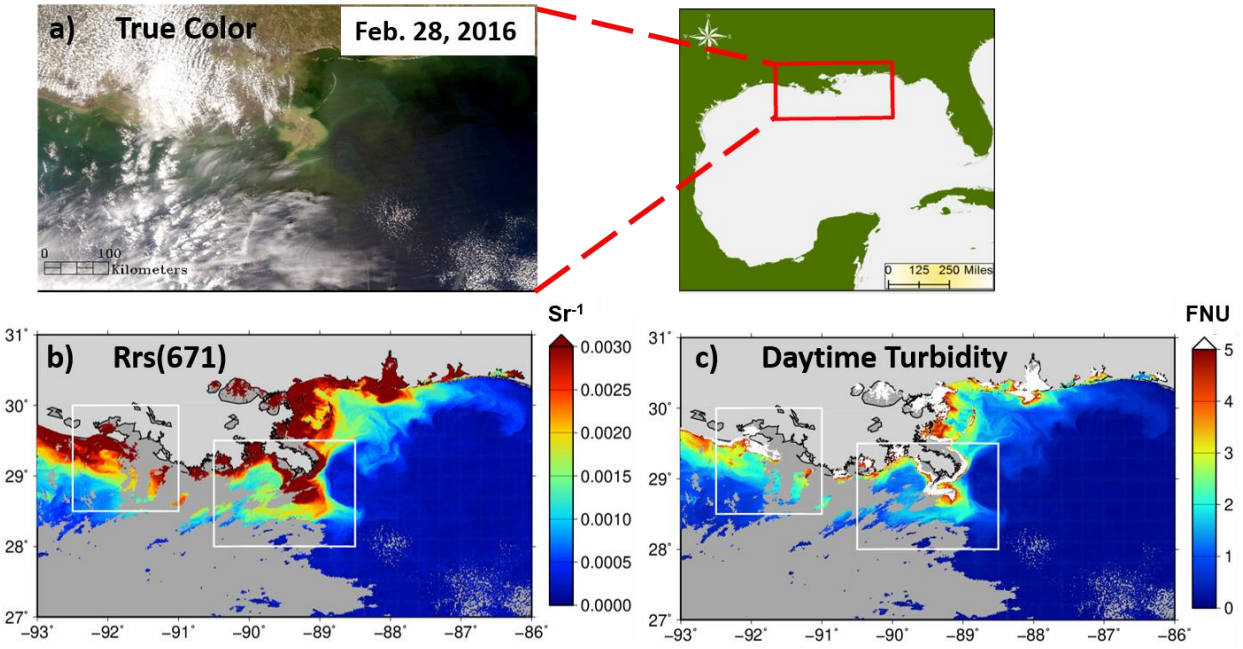

Figure 10. A sample comparison between Rrs(671) and daytime turbidity. (a) True color image, (b) Rrs(671), and (c) the derived daytime turbidity image (c) from Feb 28, 2016 over the two study areas. The unit of Rrs(671) is per steradian and the turbidity unit is FNU. The light grey area indicates land and the dark grey area marks clouds or sun-glint contaminated pixels. These grey areas are shown as the missing value in the Rrs(671) data. The missing value is labeled as “Moderate sun-glint contamination” and “Failure in any product” in the l2 flags. The detail is in the Discussion Section.

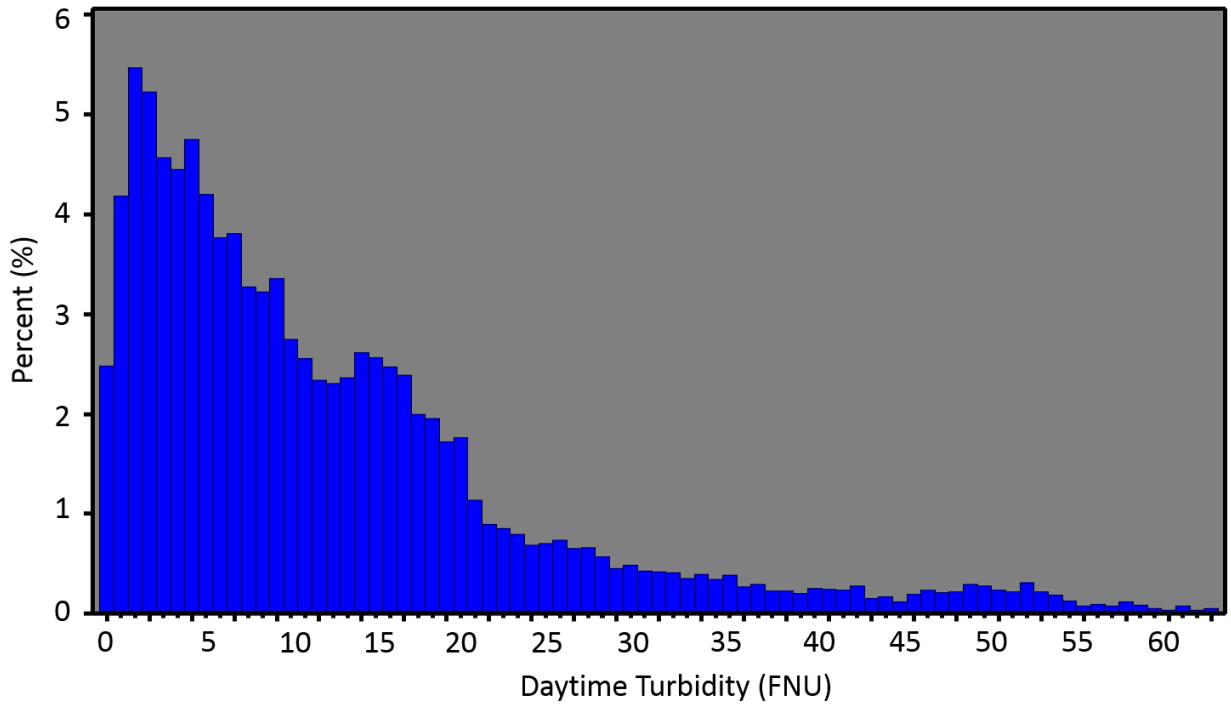

Figure 11. A distribution analysis of pixel values of daytime turbidity. The X-axis indicates turbidity value and the Y-axis is the percentage. The data are collected from the daytime turbid pixels in the 53 usable turbidity events in **Table 2**, which are then shown in **Table 7**.

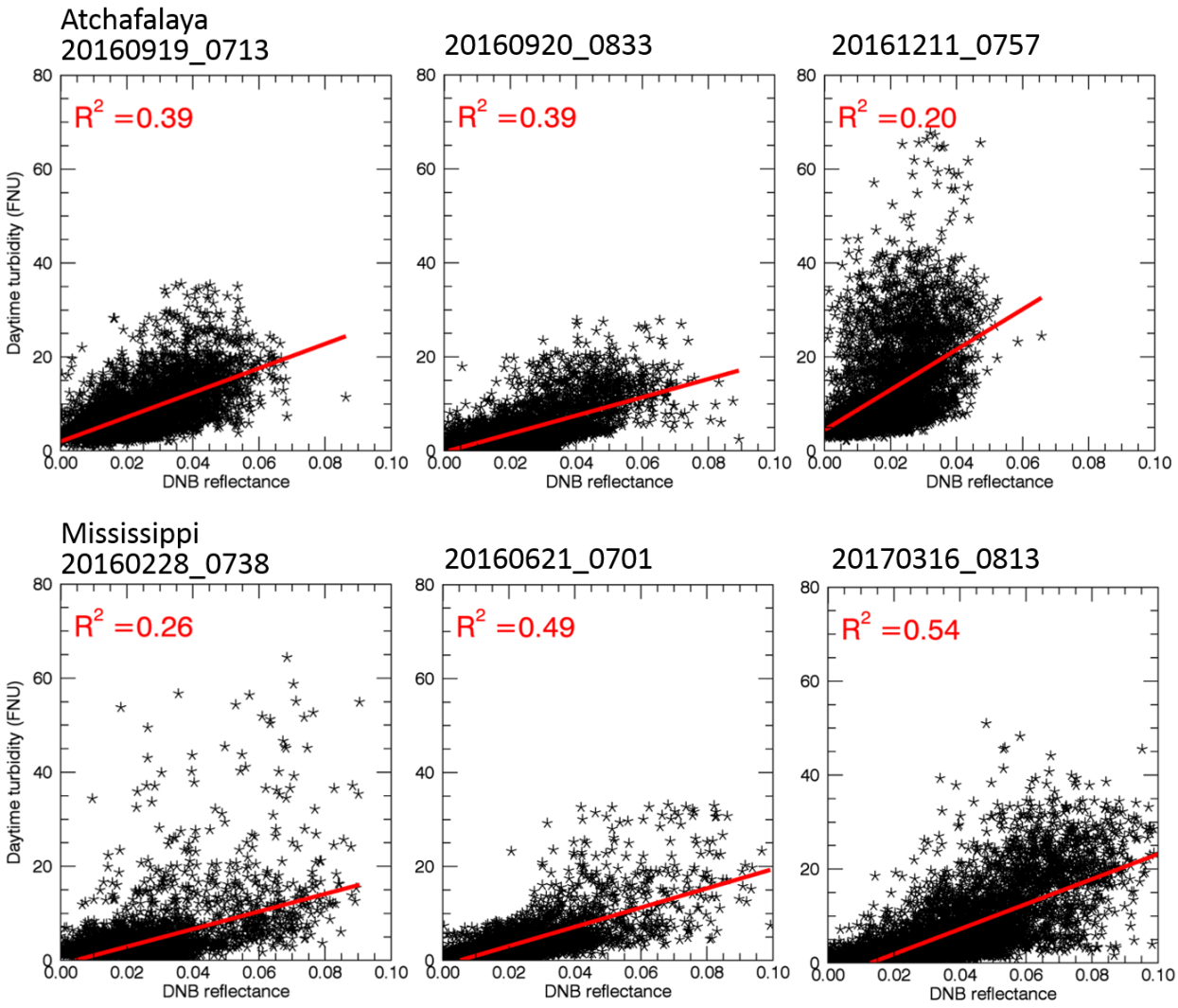

Figure 12. The scatter plot of a few cases from **Table 2** (using the Chen et al. (2007) x, y convention from their Figure 6). The X-axis is nighttime DNB reflectance and the Y-axis is VIIRS daytime turbidity. The data are paired using their location, which is a pixel-by-pixel correlation. The R^2 is labeled in the upper left corner of each panel. The red line is the best fitting line. All six figures show a poor linear correlation.

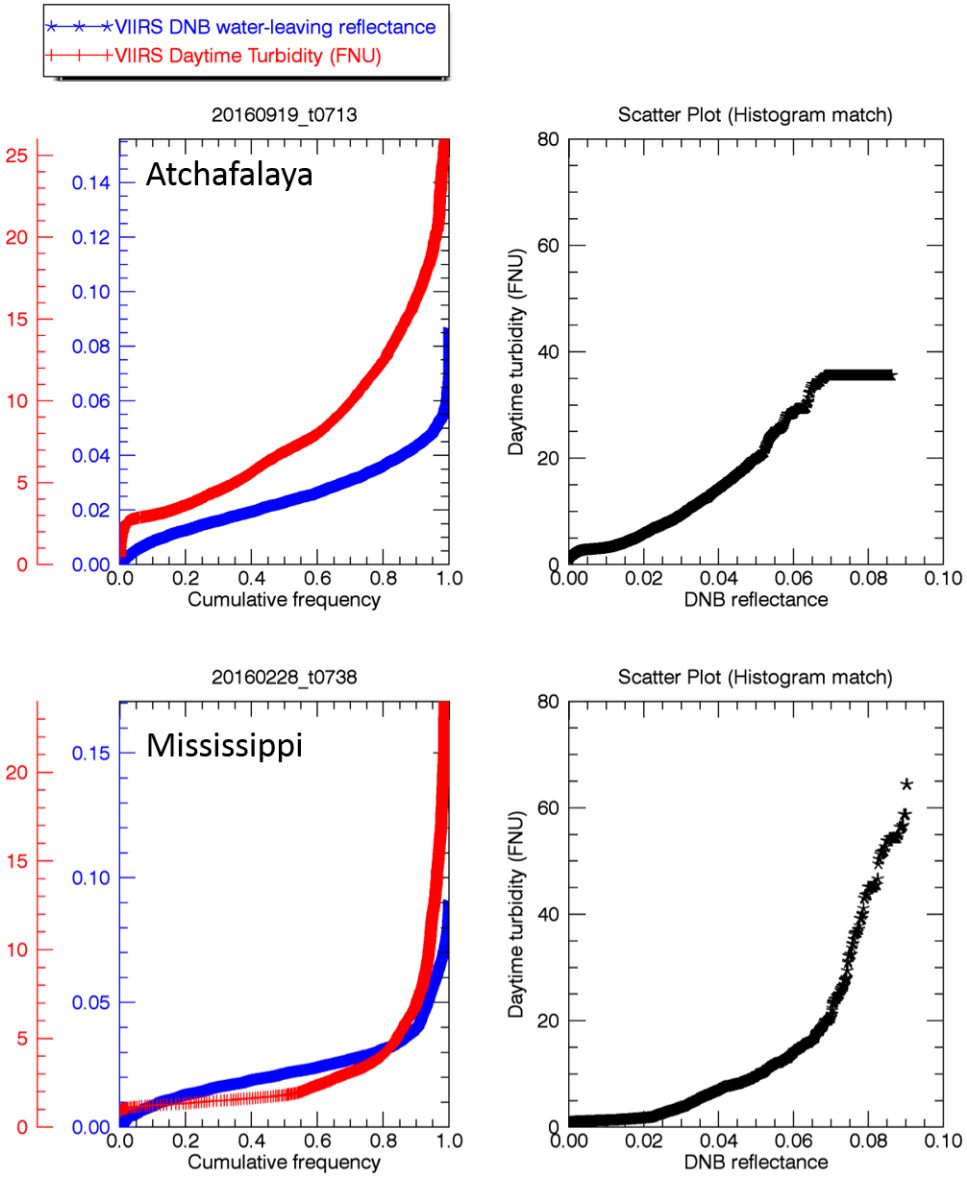

Figure 13. Examples of histogram matching. The two left panels show the cumulative histogram of nighttime DNB reflectance (blue) and VIIRS daytime turbidity (red), with the corresponding y-axis in the left. The two right panels are the scatter plot based on the frequency in the left panels. The black lines are the results of the histogram matching. The 4 panels correspond to the two of the six cases in **Figure 12**. Note that the FNU range of y-axis is different in the right and left panels. This is because, in the left panels, the y-axis only plots nighttime DNB reflectance with frequency 0.01-0.99. The y-axis changes the range according to the maximum turbidity value. For the right panels, all frequencies of data are plotted.

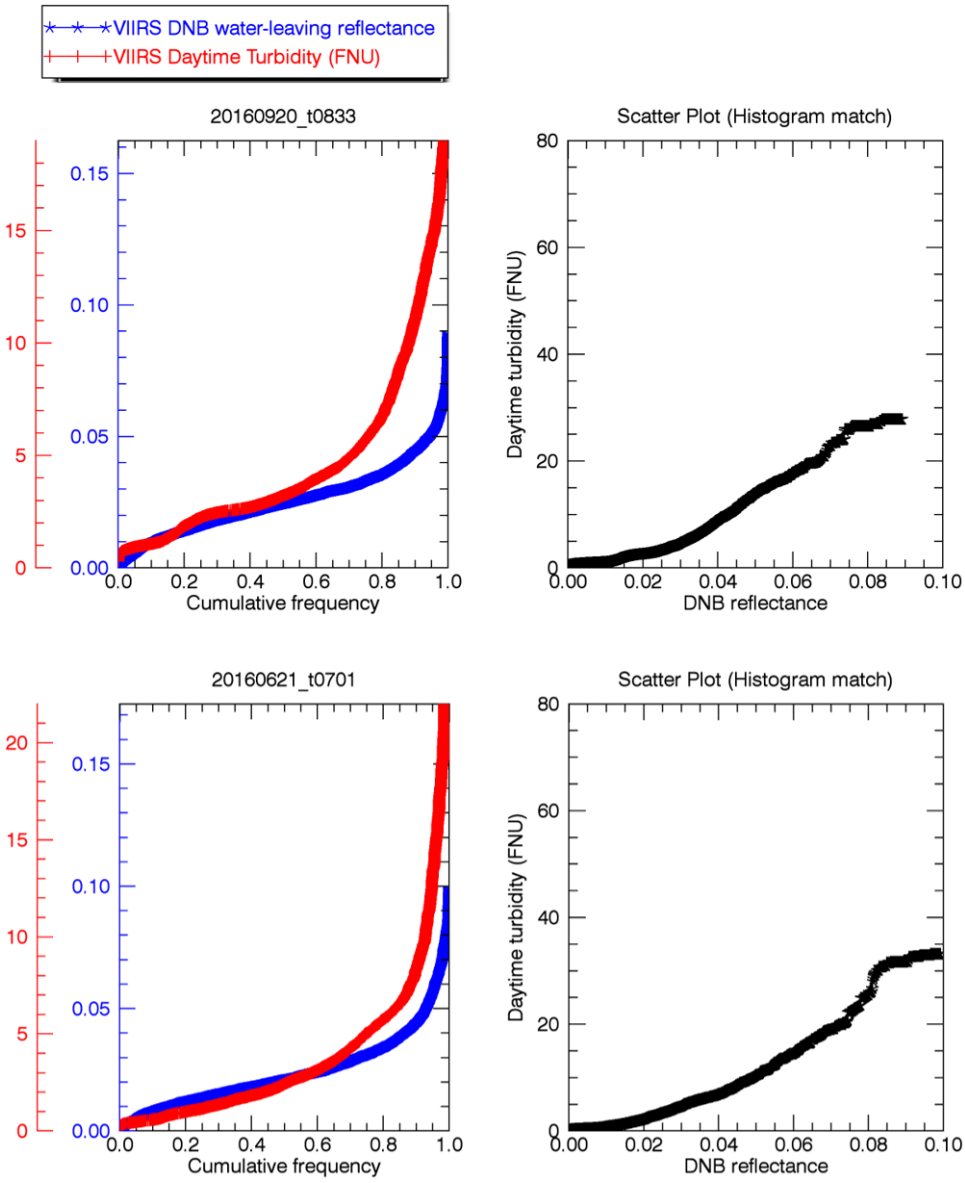

Figure 13. (Continued). Examples of histogram matching.

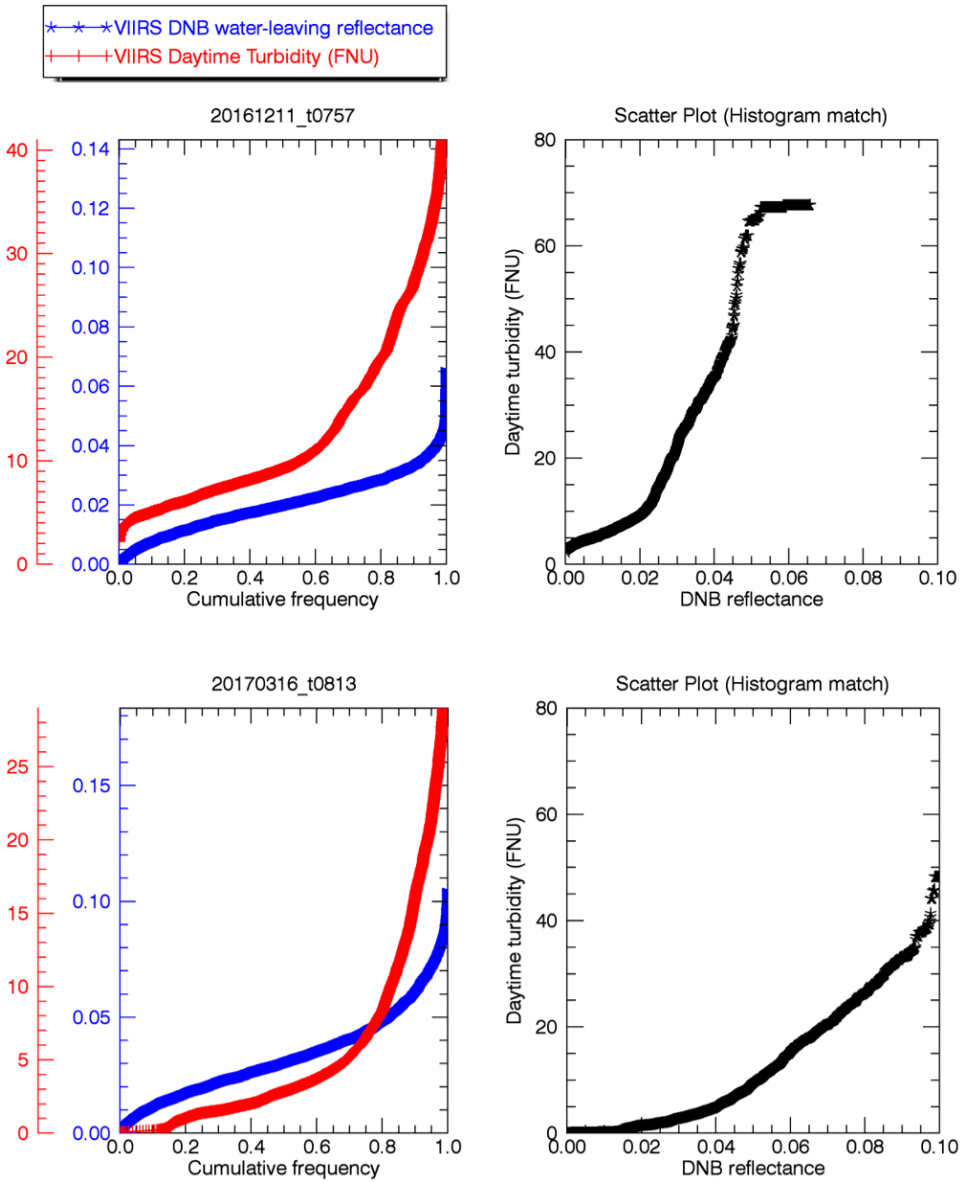

Figure 13. (Continued). Examples of histogram matching.

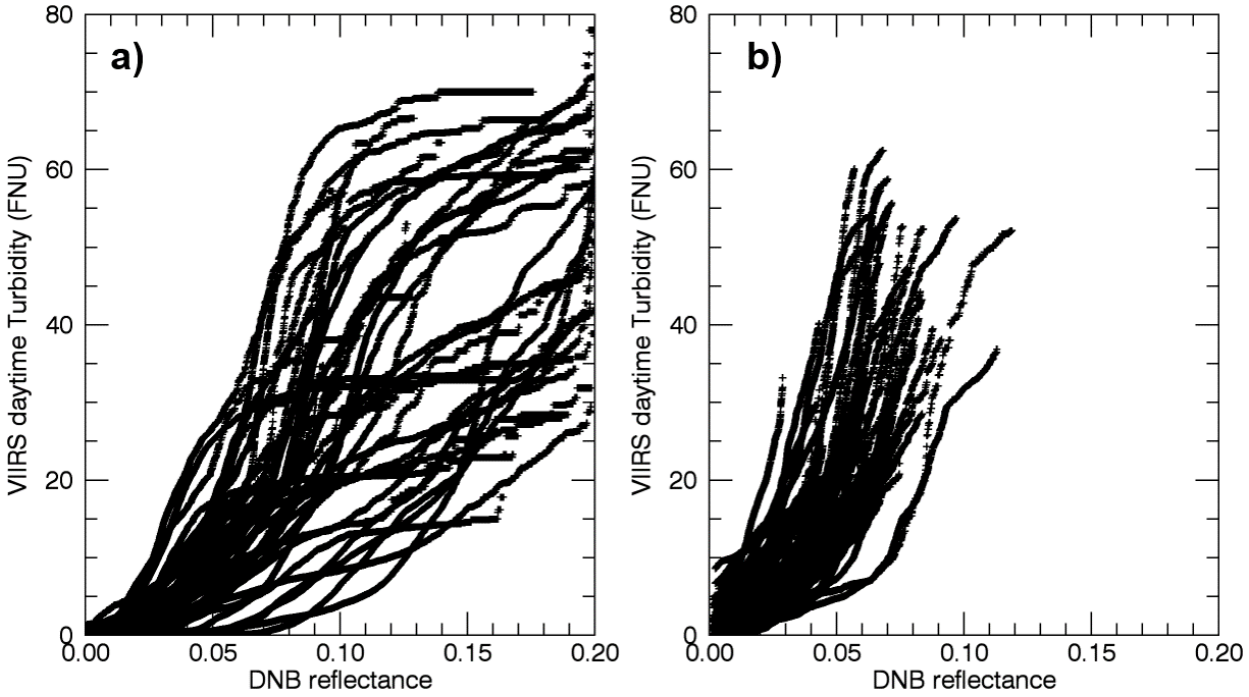

Figure 14. The scatter plots of the 86 cases ("y" cases) in **Table 2** and 53 culled cases in **Table 7**. The x, y pairing follows that of **Figure 12**. The X-axis is nighttime DNB reflectance (dimensionless) and the Y-axis indicates daytime turbidity. The black lines are the paired results of the histogram matching. (a) shows all data corresponds to **Table 2** (i.e., all "y" cases), and has not had any sieving and not separated into two study regions. For example, some lines contain the data from both study regions, as labeled "afa+miss" in **Table 2**. (b) shows the 53 cases, filtered by the satellite view angle ($<60^0$), sun-glint and moon-glint, study regions. Each line in (b) only represents the data from either the Atchafalaya Bay or the Mississippi River Delta.

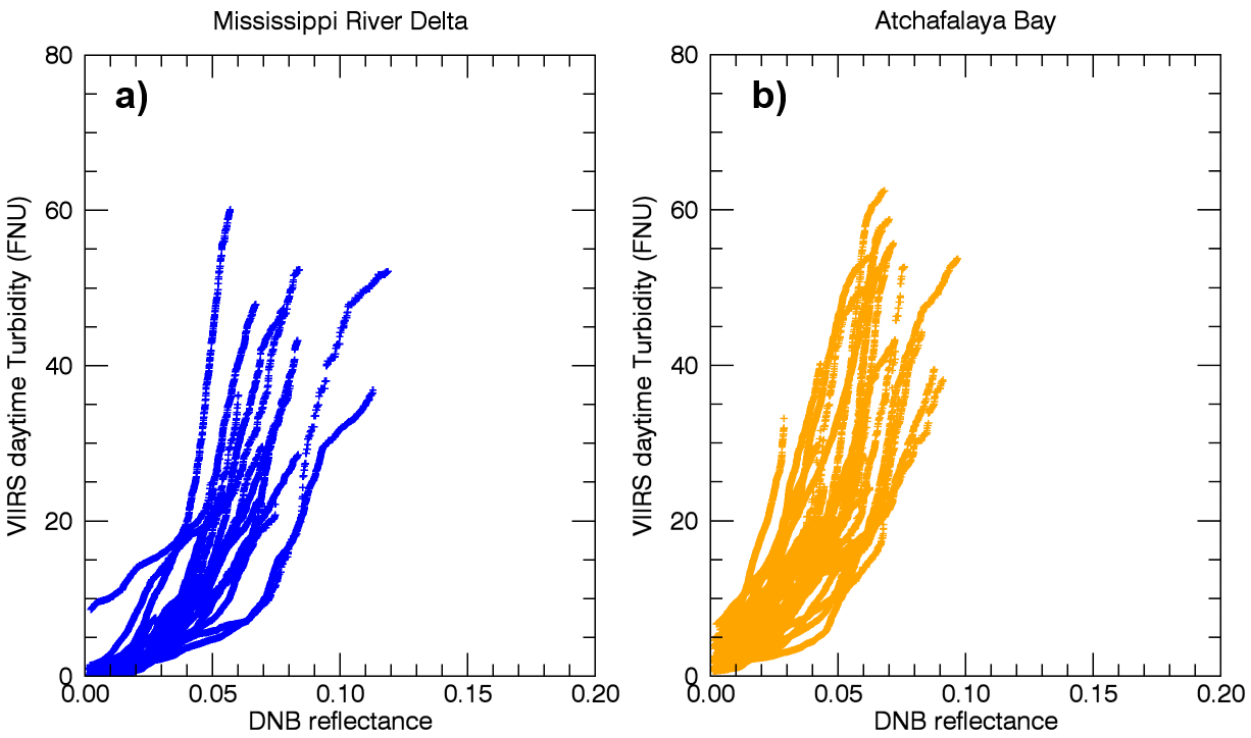

Figure 15. The comparison of the scatter plots of 53 cases (x, y pairing follows that of Figure 12). The blue and the yellow lines are the result of the histogram matching. (a) shows the valid 19 cases in the Mississippi River Delta, and (b) represents 34 cases in the Atchafalaya Bay after sieving.

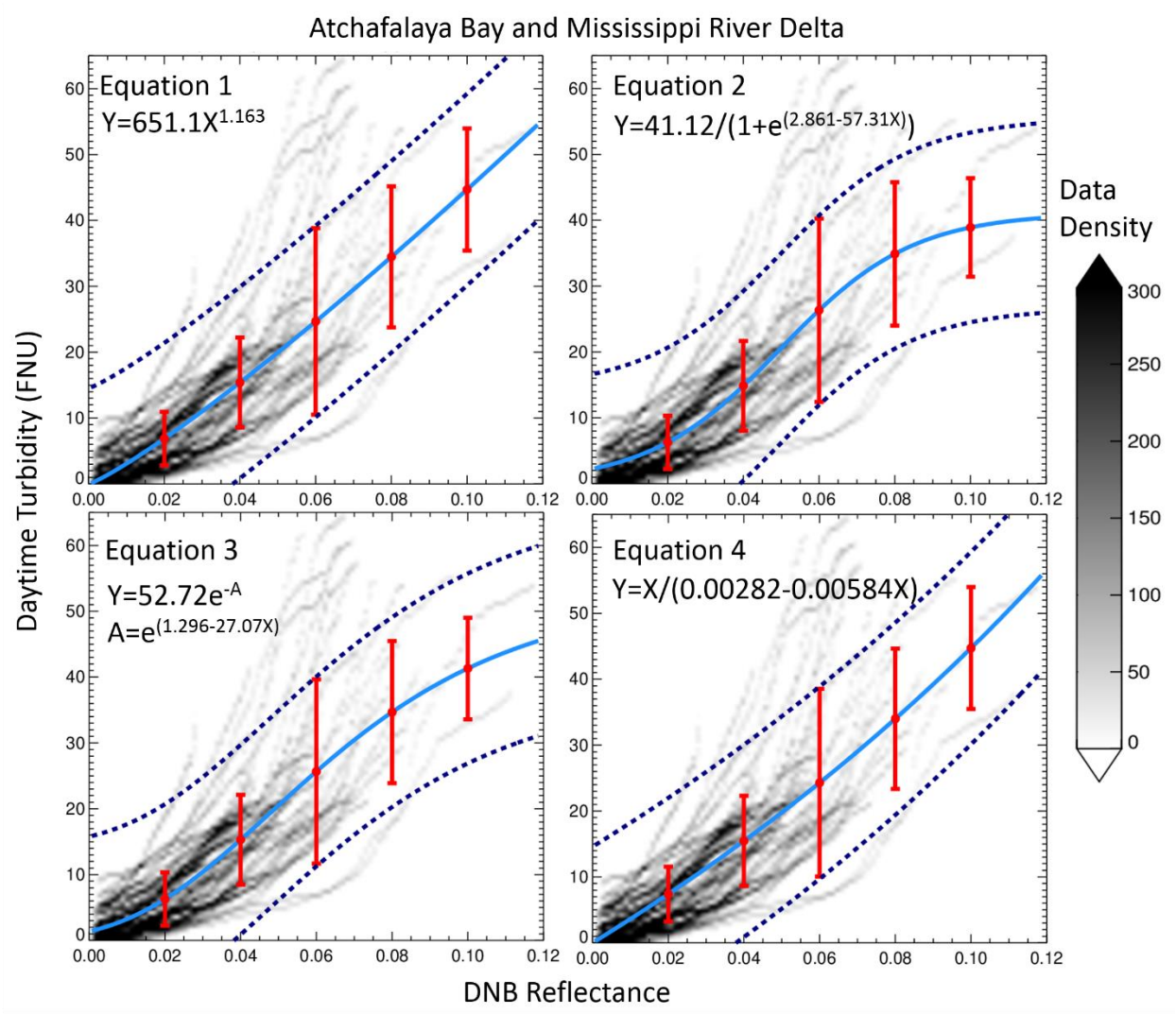

Figure 16. The comparison of the four equations fitting the 53 cases. The data is same as **Figure 14**b. The x, y pairing follows that of **Figure 12**. The x-axis is nighttime DNB reflectance and y-axis is daytime turbidity. The color bar in the right indicates the density of data. The black shaded area is with the largest amount of data. The light blue line is the best fitting line. The error bars represent the standard error of estimate. The dark blue dashed lines are the 95% prediction interval. The four equations are labeled in the upper left corner of each panel. The statistics can be checked in **Table 5** and **Table 6**.

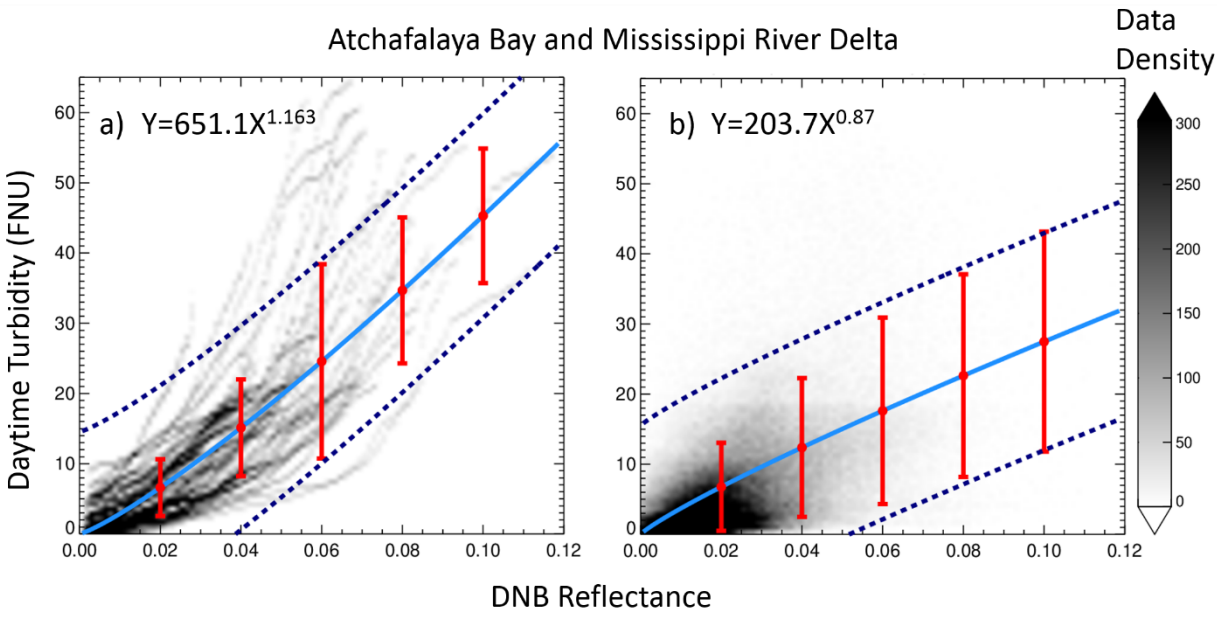

Figure 17. The comparison of two different matching methods. The x, y pairing follows that of **Figure 12**. The x-axis is nighttime DNB reflectance and y-axis is daytime turbidity. The color bar in the right indicates the density of data. The black shaded area is with the largest amount of data. The light blue line is the best fitting line. The error bars represent the standard error of estimate. The dark blue dashed lines are the 95% prediction interval. The equation is shown in the upper left corner of each panel. (a) is the equation 1 (**Figure 16**). (b) is fitted with the pixel-by-pixel matching method that strongly correlates with their locations.

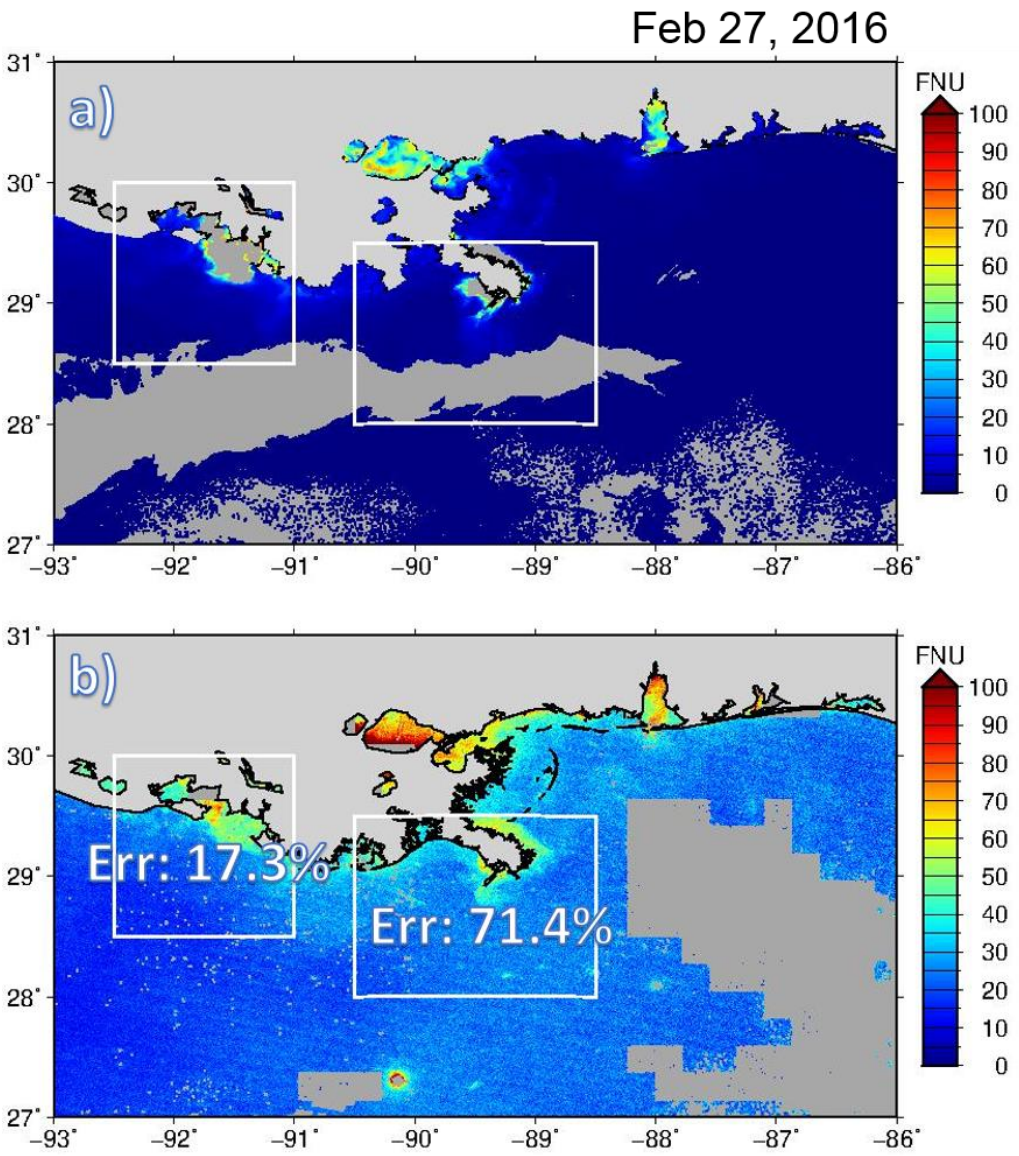

Figure 18. A case comparison of calculated daytime and nighttime turbidity. The daytime turbidity is calculated from Rrs(671) & Rrs(862). The nighttime turbidity is calculated from equation 1 (**Figure 16**). (a) shows the calculated daytime turbidity and (b) shows the calculated nighttime turbidity on February 27, 2016. Note that the nighttime calculations precede daytime calculations within a given GMT day. The two white boxes correspond to the two study regions in **Figure 1**. The figure shows the mean relative error in both study regions, with 17.3% in the Atchafalaya Bay and 71.4% in the Mississippi River Delta, respectively. The grey shaded pixels near the coastal regions are missing data. The missing data are labeled as “Moderate sun glint contamination” and “Failure in any product” in the l2 flags. The detail is in the Discussion Section.

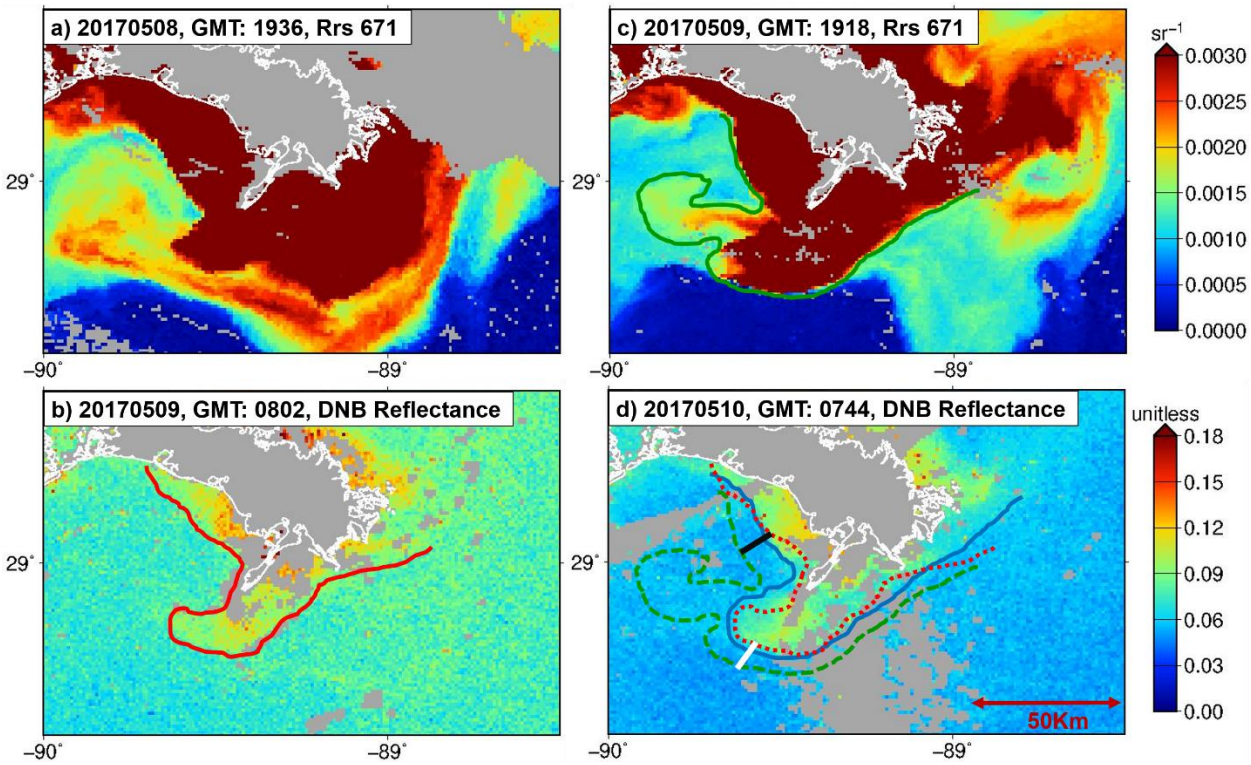

Figure 19. The changes of a sediment front position observed from daytime and nighttime data. The 4 panels illustrate an example of where a sediment front relocates in the Mississippi River mouth from May 8 to 10, 2017. (a) is the daytime Rrs(671) map on May 8, 2017 at 1936 GMT. (b) shows the nighttime DNB reflectance map on May 9, 2017 at 0802 GMT. The red solid line indicates the sediment front in the map. (c) shows the daytime Rrs(671) map on May 9, 2017 at 1918 GMT. The solid green line denotes the sediment front. (d) shows the nighttime DNB reflectance map on May 10, 2017 at 0744 GMT. The blue line denotes the sediment fronts for this time that is shown with respect to the previous red (b) and green (c) sediment front positions. The black and white solid lines in (d) show the minimum linear distance that the front moved. Note that May 10, 2017 is a full moon date.

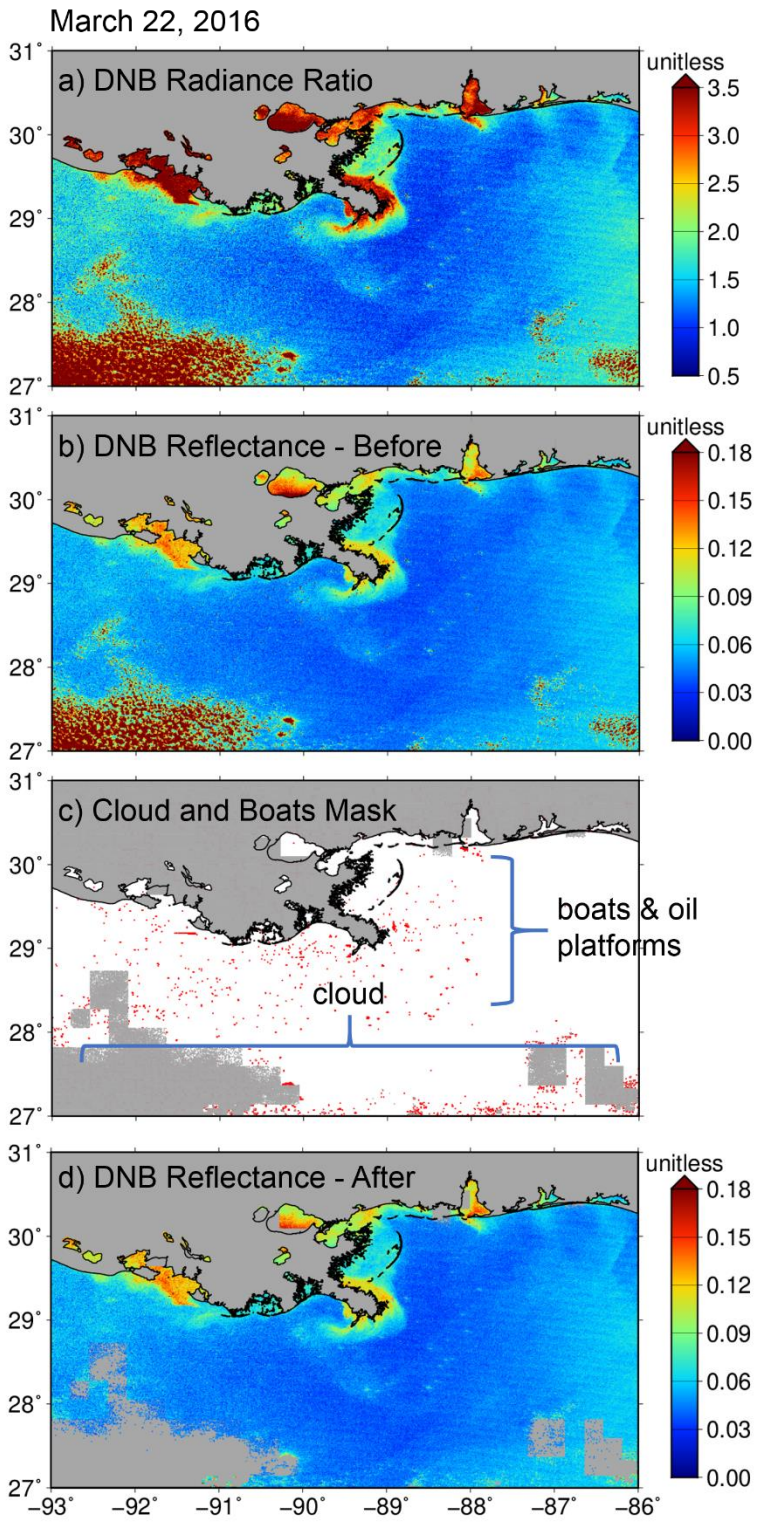

Figure 20. A comparison between nighttime DNB ratio and nighttime DNB reflectance. The chosen maps are at the same time of March 22, 2016. (a) is nighttime DNB radiance ratio map. The color shaded area in the coastal regions indicates the turbidity pattern. (b) is nighttime DNB reflectance. (c) indicates land, cloud pixels (grey), boats, and oil platforms (red). Note that some red pixels are also clouds, as labeled in the bottom of (c). (d) is the nighttime DNB reflectance map, where lands, clouds, fishing boats and oil platforms have been removed and labeled in grey color. The greenish and reddish areas near the shoreline show the turbid regions.

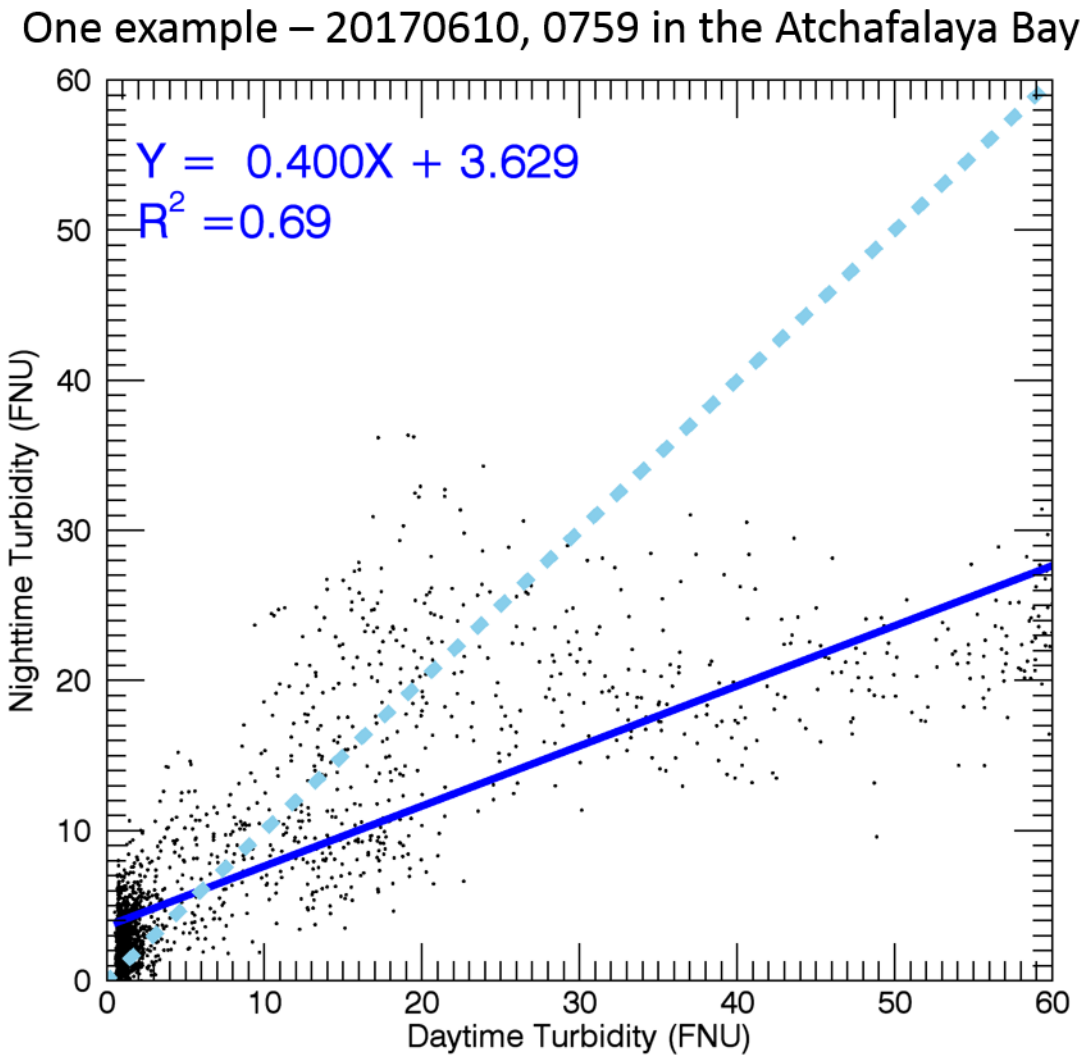

Figure 21. One example of nighttime versus daytime turbidity from **Table 7**. The case is on June, 10, 2017 at 0759 GMT in the Atchafalaya Bay. The light blue dashed-line marks a 1:1 match. The dark blue line is the linear fit by the equation shown. The linear equation and R^2 are labeled in the upper left corner.

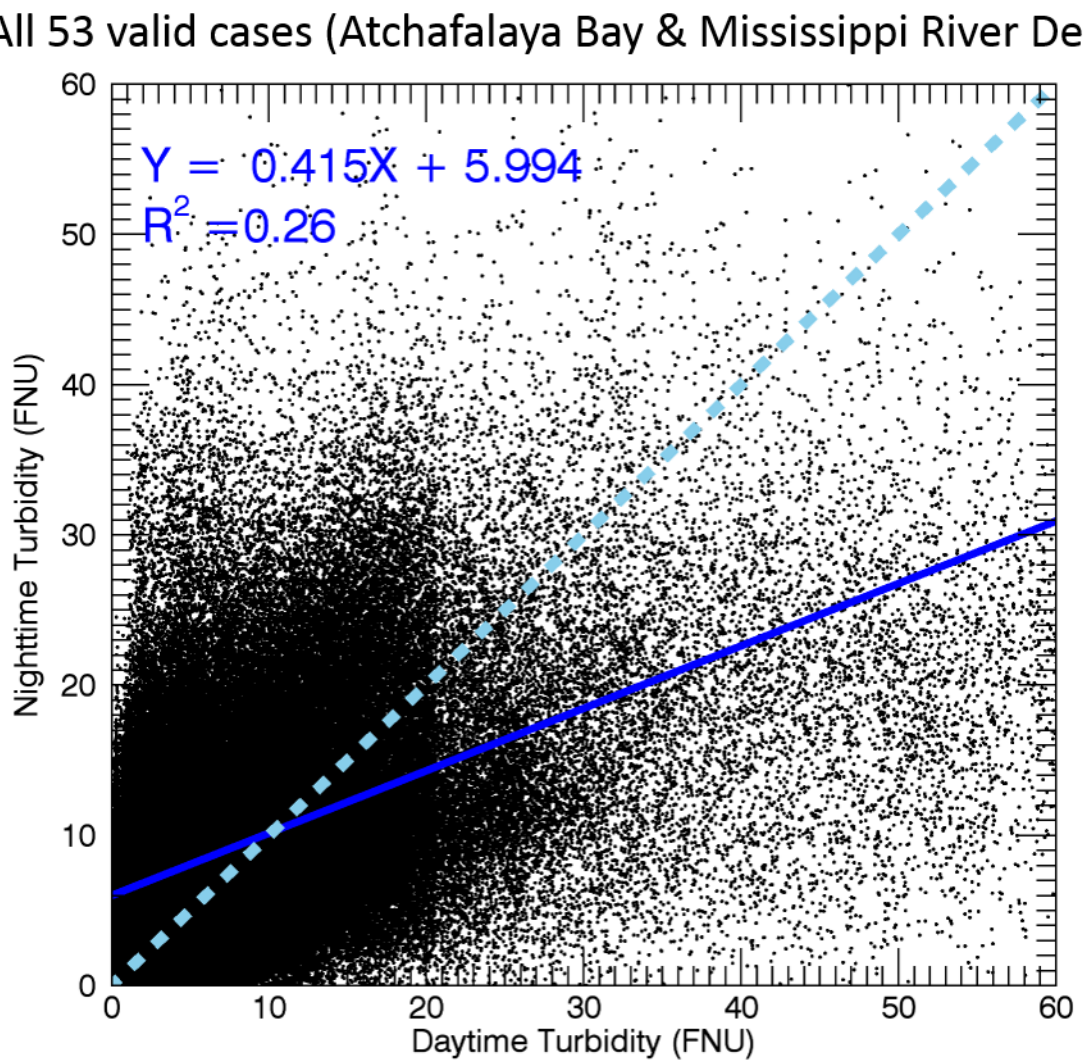

Figure 22. The nighttime turbidity versus daytime turbidity in all 53 valid cases from **Table 7**. The light blue dashed-line marks a 1:1 match. The dark blue line is the linear fit by the equation shown. The linear equation and R^2 are labeled in the upper left corner. Note that the apparent vertical boundary at 20 FNU for daytime turbidity is due to the data distribution shown in **Figure 11**.